Upper limits on gravitational wave emission from 78 radio pulsars

B. Abbott,[15] R. Abbott,[15] R. Adhikari,[15] J. Agresti,[15] P. Ajith,[2] B. Allen,[2,52] R. Amin,[19] S. B. Anderson,[15] W. G. Anderson,[52] M. Arain,[40] M. Araya,[15] H. Armandula,[15] M. Ashley,[4] S. Aston,[39] P. Aufmuth,[37] C. Aulbert,[1] S. Babak,[1] S. Ballmer,[15] H. Bantilan,[9] B. C. Barish,[15] C. Barker,[16] D. Barker,[16] B. Barr,[41] P. Barriga,[51] M. A. Barton,[41] K. Bayer,[18] K. Belczynski,[25] J. Betzwieser,[18] P. T. Beyersdorf,[28] B. Bhawal,[15] I. A. Bilenko,[22] G. Billingsley,[15] R. Biswas,[52] E. Black,[15] K. Blackburn,[15] L. Blackburn,[18] D. Blair,[51] B. Bland,[16] J. Bogenstahl,[41] L. Bogue,[17] R. Bork,[15] V. Boschi,[15] S. Bose,[54] P. R. Brady,[52] V. B. Braginsky,[22] J. E. Brau,[44] M. Brinkmann,[2] A. Brooks,[38] D. A. Brown,[7,15] A. Bullington,[31] A. Bunkowski,[2] A. Buonanno,[42] O. Burmeister,[2] D. Busby,[15] W. E. Butler,[45] R. L. Byer,[31] L. Cadonati,[18] G. Cagnoli,[41] J. B. Camp,[23] J. Cannizzo,[23] K. Cannon,[52] C. A. Cantley,[41] J. Cao,[18] L. Cardenas,[15] K. Carter,[17] M. M. Casey,[41] G. Castaldi,[47] C. Cepeda,[15] E. Chalkey,[41] P. Charlton,[10] S. Chatterji,[15] S. Chelkowski,[2] Y. Chen,[1] F. Chiadini,[46] D. Chin,[43] E. Chin,[51] J. Chow,[4] N. Christensen,[9] J. Clark,[41] P. Cochrane,[2] T. Cokelaer,[8] C. N. Colacino,[39] R. Coldwell,[40] R. Conte,[46] D. Cook,[16] T. Corbitt,[18] D. Coward,[51] D. Coyne,[15] J. D. E. Creighton,[52] T. D. Creighton,[15] R. P. Croce,[47] D. R. M. Crooks,[41] A. M. Cruise,[39] A. Cumming,[41] J. Dalrymple,[32] E. D'Ambrosio,[15] K. Danzmann,[2,37] G. Davies,[8] D. DeBra,[31] J. Degallaix,[51] M. Degree,[31] T. Demma,[47] V. Dergachev,[43] S. Desai,[33] R. DeSalvo,[15] S. Dhurandhar,[14] M. Díaz,[34] J. Dickson,[4] A. Di Credico,[32] G. Diederichs,[37] A. Dietz,[8] E. E. Doomes,[30] R. W. P. Drever,[5] J.-C. Dumas,[51] R. J. Dupuis,[15] J. G. Dwyer,[11] P. Ehrens,[15] E. Espinoza,[15] T. Etzel,[15] M. Evans,[15] T. Evans,[17] S. Fairhurst,[8,15] Y. Fan,[51] D. Fazi,[15] M. M. Fejer,[31] L. S. Finn,[33] V. Fiumara,[46] N. Fotopoulos,[52] A. Franzen,[37] K. Y. Franzen,[40] A. Freise,[39] R. Frey,[44] T. Fricke,[45] P. Fritschel,[18] V. V. Frolov,[17] M. Fyffe,[17] V. Galdi,[47] K. S. Ganezer,[6] J. Garofoli,[16] I. Gholami,[1] J. A. Giaime,[17,19] S. Giampanis,[45] K. D. Giardina,[17] K. Goda,[18] E. Goetz,[43] L. Goggin,[15] G. González,[19] S. Gossler,[4] A. Grant,[41] S. Gras,[51] C. Gray,[16] M. Gray,[4] J. Greenhalgh,[27] A. M. Gretarsson,[12] R. Grosso,[34] H. Grote,[2] S. Grunewald,[1] M. Guenther,[16] R. Gustafson,[43] B. Hage,[37] D. Hammer,[52] C. Hanna,[19] J. Hanson,[17] J. Harms,[2] G. Harry,[18] E. Harstad,[44] T. Hayler,[27] J. Heefner,[15] I. S. Heng,[41] A. Heptonstall,[41] M. Heurs,[2] M. Hewitson,[2] S. Hild,[37] E. Hirose,[32] D. Hoak,[17] D. Hosken,[38] J. Hough,[41] E. Howell,[51] D. Hoyland,[39] S. H. Huttner,[41] D. Ingram,[16] E. Innerhofer,[18] M. Ito,[44] Y. Itoh,[52] A. Ivanov,[15] D. Jackrel,[31] B. Johnson,[16] W. W. Johnson,[19] D. I. Jones,[48] G. Jones,[8] R. Jones,[41] L. Ju,[51] P. Kalmus,[11] V. Kalogera,[25] D. Kasprzyk,[39] E. Katsavounidis,[18] K. Kawabe,[16] S. Kawamura,[24] F. Kawazoe,[24] W. Kells,[15] D. G. Keppel,[15] F. Ya. Khalili,[22] C. Kim,[25] P. King,[15] J. S. Kissel,[19] S. Klimenko,[40] K. Kokeyama,[24] V. Kondrashov,[15] R. K. Kopparapu,[19] D. Kozak,[15] B. Krishnan,[1] P. Kwee,[37] P. K. Lam,[4] M. Landry,[16] B. Lantz,[31] A. Lazzarini,[15] B. Lee,[51] M. Lei,[15] J. Leiner,[54] V. Leonhardt,[24] I. Leonor,[44] K. Libbrecht,[15] P. Lindquist,[15] N. A. Lockerbie,[49] M. Longo,[46] M. Lormand,[17] M. Lubinski,[16] H. Lück,[2,37] B. Machenschalk,[1] M. MacInnis,[18] M. Mageswaran,[15] K. Mailand,[15] M. Malec,[37] V. Mandic,[15] S. Marano,[46] S. Márka,[11] J. Markowitz,[18] E. Maros,[15] I. Martin,[41] J. N. Marx,[15] K. Mason,[18] L. Matone,[11] V. Matta,[46] N. Mavalvala,[18] R. McCarthy,[16] D. E. McClelland,[4] S. C. McGuire,[30] M. McHugh,[21] K. McKenzie,[4] J. W. C. McNabb,[33] S. McWilliams,[23] T. Meier,[37] A. Melissinos,[45] G. Mendell,[16] R. A. Mercer,[40] S. Meshkov,[15] E. Messaritaki,[15] C. J. Messenger,[41] D. Meyers,[15] E. Mikhailov,[18] S. Mitra,[14] V. P. Mitrofanov,[22] G. Mitselmakher,[40] R. Mittleman,[18] O. Miyakawa,[15] S. Mohanty,[34] G. Moreno,[16] K. Mossavi,[2] C. MowLowry,[4] A. Moylan,[4] D. Mudge,[38] G. Mueller,[40] S. Mukherjee,[34] H. Müller-Ebhardt,[2] J. Munch,[38] P. Murray,[41] E. Myers,[16] J. Myers,[16] T. Nash,[15] G. Newton,[41] A. Nishizawa,[24] F. Nocera,[15] K. Numata,[23] B. O'Reilly,[17] R. O'Shaughnessy,[25] D. J. Ottaway,[18] H. Overmier,[17] B. J. Owen,[33] Y. Pan,[42] M. A. Papa,[1,52] V. Parameshwaraiah,[16] C. Parameswariah,[17] P. Patel,[15] M. Pedraza,[15] S. Penn,[13] V. Pierro,[47] I. M. Pinto,[47] M. Pitkin,[41,*] H. Pletsch,[2] M. V. Plissi,[41] F. Postiglione,[46] R. Prix,[1] V. Quetschke,[40] F. Raab,[16] D. Rabeling,[4] H. Radkins,[16] R. Rahkola,[44] N. Rainer,[2] M. Rakhmanov,[33] K. Rawlins,[18] S. Ray-Majumder,[52] V. Re,[39] T. Regimbau,[8] H. Rehbein,[2] S. Reid,[41] D. H. Reitze,[40] L. Ribichini,[2] R. Riesen,[17] K. Riles,[43] B. Rivera,[16] N. A. Robertson,[15,41] C. Robinson,[8] E. L. Robinson,[39] S. Roddy,[17] A. Rodriguez,[19] A. M. Rogan,[54] J. Rollins,[11] J. D. Romano,[8] J. Romie,[17] R. Route,[31] S. Rowan,[41] A. Rüdiger,[2] L. Ruet,[18] P. Russell,[15] K. Ryan,[16] S. Sakata,[24] M. Samidi,[15] L. Sancho de la Jordana,[36] V. Sandberg,[16] G. H. Sanders,[15] V. Sannibale,[15] S. Saraf,[26] P. Sarin,[18] B. S. Sathyaprakash,[8] S. Sato,[24] P. R. Saulson,[32] R. Savage,[16] P. Savov,[7] A. Sazonov,[40] S. Schediwy,[51] R. Schilling,[2] R. Schnabel,[2] R. Schofield,[44] B. F. Schutz,[1,8] P. Schwinberg,[16] S. M. Scott,[4] A. C. Searle,[4] B. Sears,[15] F. Seifert,[2] D. Sellers,[17] A. S. Sengupta,[8] P. Shawhan,[42] D. H. Shoemaker,[18] A. Sibley,[17] J. A. Sidles,[50] X. Siemens,[7,15] D. Sigg,[16] S. Sinha,[31] A. M. Sintes,[1,36] B. J. J. Slagmolen,[4] J. Slutsky,[19] J. R. Smith,[2] M. R. Smith,[15] K. Somiya,[1,2] K. A. Strain,[41] D. M. Strom,[44] A. Stuver,[33] T. Z. Summerscales,[3] K.-X. Sun,[31] M. Sung,[19] P. J. Sutton,[15] H. Takahashi,[1] D. B. Tanner,[40] M. Tarallo,[15] R. Taylor,[15] R. Taylor,[41] J. Thacker,[17] K. A. Thorne,[33] K. S. Thorne,[7] A. Thüring,[37] K. V. Tokmakov,[41] C. Torres,[34] C. Torrie,[41] G. Traylor,[17] M. Trias,[36] W. Tyler,[15] D. Ugolini,[35] C. Ungarelli,[39] K. Urbanek,[31] H. Vahlbruch,[37]

M. Vallisneri,[7] C. Van Den Broeck,[8] M. van Putten,[18] M. Varvella,[15] S. Vass,[15] A. Vecchio,[39] J. Veitch,[41] P. Veitch,[38] A. Villar,[15] C. Vorvick,[16] S. P. Vyachanin,[22] S. J. Waldman,[15] L. Wallace,[15] H. Ward,[41] R. Ward,[15] K. Watts,[17] D. Webber,[15] A. Weidner,[2] M. Weinert,[2] A. Weinstein,[15] R. Weiss,[18] S. Wen,[19] K. Wette,[4] J. T. Whelan,[1] D. M. Whitbeck,[33] S. E. Whitcomb,[15] B. F. Whiting,[40] S. Wiley,[6] C. Wilkinson,[16] P. A. Willems,[15] L. Williams,[40] B. Willke,[2,37] I. Wilmut,[27] W. Winkler,[2] C. C. Wipf,[18] S. Wise,[40] A. G. Wiseman,[52] G. Woan,[41] D. Woods,[52] R. Wooley,[17] J. Worden,[16] W. Wu,[40] I. Yakushin,[17] H. Yamamoto,[15] Z. Yan,[51] S. Yoshida,[29] N. Yunes,[33] M. Zanolin,[18] J. Zhang,[43] L. Zhang,[15] C. Zhao,[51] N. Zotov,[20] M. Zucker,[18] H. zur Mühlen,[37] and J. Zweizig[15]

(LIGO Scientific Collaboration)

[1]*Albert-Einstein-Institut, Max-Planck-Institut für Gravitationsphysik, D-14476 Golm, Germany*
[2]*Albert-Einstein-Institut, Max-Planck-Institut für Gravitationsphysik, D-30167 Hannover, Germany*
[3]*Andrews University, Berrien Springs, Michigan 49104 USA*
[4]*Australian National University, Canberra, 0200, Australia*
[5]*California Institute of Technology, Pasadena, California 91125, USA*
[6]*California State University Dominguez Hills, Carson, California 90747, USA*
[7]*Caltech-CaRT, Pasadena, California 91125, USA*
[8]*Cardiff University, Cardiff, CF2 3YB, United Kingdom*
[9]*Carleton College, Northfield, Minnesota 55057, USA*
[10]*Charles Sturt University, Wagga Wagga, NSW 2678, Australia*
[11]*Columbia University, New York, New York 10027, USA*
[12]*Embry-Riddle Aeronautical University, Prescott, Arizona 86301 USA*
[13]*Hobart and William Smith Colleges, Geneva, New York 14456, USA*
[14]*Inter-University Centre for Astronomy and Astrophysics, Pune–411007, India*
[15]*LIGO–California Institute of Technology, Pasadena, California 91125, USA*
[16]*LIGO Hanford Observatory, Richland, Washington 99352, USA*
[17]*LIGO Livingston Observatory, Livingston, Louisiana 70754, USA*
[18]*LIGO–Massachusetts Institute of Technology, Cambridge, Massachusetts 02139, USA*
[19]*Louisiana State University, Baton Rouge, Louisiana 70803, USA*
[20]*Louisiana Tech University, Ruston, Louisiana 71272, USA*
[21]*Loyola University, New Orleans, Louisiana 70118, USA*
[22]*Moscow State University, Moscow, 119992, Russia*
[23]*NASA/Goddard Space Flight Center, Greenbelt, Maryland 20771, USA*
[24]*National Astronomical Observatory of Japan, Tokyo 181-8588, Japan*
[25]*Northwestern University, Evanston, Illinois 60208, USA*
[26]*Rochester Institute of Technology, Rochester, New York 14623, USA*
[27]*Rutherford Appleton Laboratory, Chilton, Didcot, Oxon OX11 0QX United Kingdom*
[28]*San Jose State University, San Jose, California 95192, USA*
[29]*Southeastern Louisiana University, Hammond, Louisiana 70402, USA*
[30]*Southern University and A&M College, Baton Rouge, Louisiana 70813, USA*
[31]*Stanford University, Stanford, California 94305, USA*
[32]*Syracuse University, Syracuse, New York 13244, USA*
[33]*The Pennsylvania State University, University Park, Pennsylvania 16802, USA*
[34]*The University of Texas at Brownsville and Texas Southmost College, Brownsville, Texas 78520, USA*
[35]*Trinity University, San Antonio, Texas 78212, USA*
[36]*Universitat de les Illes Balears, E-07122 Palma de Mallorca, Spain*
[37]*Universität Hannover, D-30167 Hannover, Germany*
[38]*University of Adelaide, Adelaide, SA 5005, Australia*
[39]*University of Birmingham, Birmingham, B15 2TT, United Kingdom*
[40]*University of Florida, Gainesville, Florida 32611, USA*
[41]*University of Glasgow, Glasgow, G12 8QQ, United Kingdom*
[42]*University of Maryland, College Park, Maryland 20742 USA*
[43]*University of Michigan, Ann Arbor, Michigan 48109, USA*
[44]*University of Oregon, Eugene, Oregon 97403, USA*
[45]*University of Rochester, Rochester, New York 14627, USA*
[46]*University of Salerno, 84084 Fisciano (Salerno), Italy*
[47]*University of Sannio at Benevento, I-82100 Benevento, Italy*
[48]*University of Southampton, Southampton, SO17 1BJ, United Kingdom*
[49]*University of Strathclyde, Glasgow, G1 1XQ, United Kingdom*

[50]University of Washington, Seattle, Washington, 98195, USA
[51]University of Western Australia, Crawley, WA 6009, Australia
[52]University of Wisconsin-Milwaukee, Milwaukee, Wisconsin 53201, USA
[53]Vassar College, Poughkeepsie, New York 12604, USA
[54]Washington State University, Pullman, Washington 99164, USA

M. Kramer and A. G. Lyne

University of Manchester, Jodrell Bank Observatory, Macclesfield, SK11 9DL, United Kingdom
(Received 4 April 2007; revised manuscript received 20 June 2007; published 3 August 2007; publisher error corrected 29 February 2008)

We present upper limits on the gravitational wave emission from 78 radio pulsars based on data from the third and fourth science runs of the LIGO and GEO 600 gravitational wave detectors. The data from both runs have been combined coherently to maximize sensitivity. For the first time, pulsars within binary (or multiple) systems have been included in the search by taking into account the signal modulation due to their orbits. Our upper limits are therefore the first measured for 56 of these pulsars. For the remaining 22, our results improve on previous upper limits by up to a factor of 10. For example, our tightest upper limit on the gravitational strain is 2.6×10^{-25} for PSR J1603 − 7202, and the equatorial ellipticity of PSR J2124–3358 is less than 10^{-6}. Furthermore, our strain upper limit for the Crab pulsar is only 2.2 times greater than the fiducial spin-down limit.

DOI: 10.1103/PhysRevD.76.042001 PACS numbers: 04.80.Nn, 07.05.Kf, 95.55.Ym, 97.60.Gb

I. INTRODUCTION

This paper details the results of a search for gravitational wave signals from known radio pulsars in data from the third and fourth LIGO and GEO 600 science runs (denoted S3 and S4). These runs were carried out from 31 October 2003 to 9 January 2004 and from 22 February 2005 to 23 March 2005, respectively. We have applied, and extended, the search technique of Dupuis and Woan [1] to generate upper limits on the gravitational wave amplitude from a selection of known radio pulsars, and infer upper limits on their equatorial ellipticities. The work is a natural extension of our previous work given in Refs. [2,3].

A. Motivation

To emit gravitational waves a pulsar must have some mass (or mass-current) asymmetry around its rotation axis. This can be achieved through several mechanisms such as elastic deformations of the solid crust or core or distortion of the entire star by an extremely strong misaligned magnetic field (see Sec. III of Ref. [4] for a recent review). Such mechanisms generally result in a triaxial neutron star which, in the quadrupole approximation and with rotation and angular momentum axes aligned, would produce gravitational waves at twice the rotation frequency. These waves would have a characteristic strain amplitude at the Earth (assuming optimal orientation of the rotation axis) of

$$h_0 = \frac{16\pi^2 G}{c^4}\frac{\varepsilon I_{zz}\nu^2}{r}, \tag{1.1}$$

where ν is the neutron star's spin frequency, I_{zz} its principal moment of inertia, $\varepsilon = (I_{xx} - I_{yy})/I_{zz}$ its equatorial ellipticity, and r its distance from Earth [5].

A rotating neutron star may also emit gravitational waves at frequencies other than 2ν. For instance, if the star is undergoing free precession there will be gravitational wave emission at (or close to) both ν and 2ν [6]. In general, such a precession would modulate the time of arrival of the radio pulses. No strong evidence of such a modulation is seen in any of the pulsars within our search band, although it might go unnoticed by radio astronomers, either because the modulation is small (as would be the case if the precession is occurring about an axis close to the pulsar beam axis) or because the period of the modulation is very long. However, this misalignment and precession will be quickly damped unless sustained by some mechanism (e.g. Ref. [7]), and even with such a mechanism, calculations give strain amplitudes which would probably be too low compared to LIGO sensitivities [7,8]. For these reasons, and for the reason discussed in Sec. III, we restrict our search to twice the rotation frequency. Of course, it cannot be ruled out that there are in fact other gravitational wave components, perhaps caused either by a stronger than expected precession excitation mechanism or by an event in the pulsar's recent past that has set it into a precessional motion which has not yet decayed away. A search for gravitational waves from the Crab pulsar at frequencies other than twice the rotation frequency is currently under way and will be presented elsewhere.

Known pulsars provide an enticing target for gravitational wave searches as their positions and frequencies are generally well known through radio or x-ray observations. As a result the signal search covers a much smaller parameter space than is necessary when searching for signals from unknown sources, giving a lower significance threshold. In addition, the deterministic nature of the waves allows a building up of the signal-to-noise ratio by observing coherently for a considerable time. The main drawback in a search for gravitational waves from the majority of

*matthew@astro.gla.ac.uk

known pulsars is that the level of emission is likely to be lower than can be detected with current detector sensitivities.

Using existing radio measurements, and some reasonable assumptions, it is possible to set an upper limit on the gravitational wave amplitude from a pulsar based purely on energy conservation arguments. If one assumes that the pulsar is an isolated rigid body and that the observed spin-down of the pulsar is due to the loss of rotational kinetic energy as gravitational radiation (i.e., $\mathrm{d}E_{\mathrm{rot}}/\mathrm{d}t = 4\pi^2 I_{zz}\nu\dot{\nu}$), then the gravitational wave amplitude at the Earth (assuming optimal orientation of the rotation axis) would be

$$h_{\mathrm{sd}} = \left(\frac{5}{2}\frac{GI_{zz}|\dot{\nu}|}{c^3 r^2 \nu}\right)^{1/2}. \tag{1.2}$$

Of course these assumptions may not hold, but it would be surprising if neutron stars radiated significantly more gravitational energy than this. With these uncertainties in mind, searches such as the one described in this paper place *direct* upper limits on gravitational wave emission from rotating neutron stars, and these limits are already approaching the regime of astrophysical interest.

B. Previous results

Before the advent of large-scale interferometric detectors, there was only a limited ability to search for gravitational waves from known pulsars. Resonant mass gravitational wave detectors are only sensitive in a relatively narrow band around their resonant frequency and so cannot be used to target objects radiating outside that band. A specific attempt to search for gravitational waves from the Crab pulsar at a frequency of ~60 Hz was, however, made with a specially designed aluminum quadrupole antenna [9,10] giving a 1σ upper limit of $h_0 \leq 2 \times 10^{-22}$. A search for gravitational waves from what was then the fastest millisecond pulsar, PSR J1939 + 2134, was conducted by Hough *et al.* [11] using a split bar detector, producing an upper limit of $h_0 < 10^{-20}$.

The first pulsar search using interferometer data was carried out with the prototype 40 m interferometer at Caltech by Hereld [12]. The search was again for gravitational waves from PSR J1939 + 2134, and produced upper limits of $h_0 < 3.1 \times 10^{-17}$ and $h_0 < 1.5 \times 10^{-17}$ for the first and second harmonics of the pulsar's rotation frequency.

A much larger sample of pulsars is accessible to broadband interferometers. As of the beginning of 2005 the Australia Telescope National Facility (ATNF) online pulsar catalogue [13] listed[1] 154 millisecond and young pulsars, all with rotation frequencies >25 Hz (gravitational wave frequency >50 Hz) that fall within the design band of the LIGO and GEO 600 interferometers, and the search for their gravitational waves has developed rapidly since the start of data-taking runs in 2002. Data from the first science run (S1) were used to perform a search for gravitational waves at twice the rotation frequency from PSR J1939 + 2134 [2]. Two techniques were used in this search: one a frequency domain, frequentist search, and the other a time domain, Bayesian search which gave a 95% credible amplitude upper limit of 1.4×10^{-22}, and an ellipticity upper limit of 2.9×10^{-4} assuming $I_{zz} = 10^{38}\ \mathrm{kg\,m^2}$.

Analysis of data from the LIGO S2 science run set upper limits on the gravitational wave amplitude from 28 radio pulsars [3]. To do this, new radio timing data were obtained to ensure the pulsars' rotational phases could be predicted with the necessary accuracy and to check that none of the pulsars had glitched. These data gave strain upper limits as low as a few times 10^{-24}, and several ellipticity upper limits less than 10^{-5}. The Crab pulsar was also studied in this run, giving an upper limit a factor of ~30 greater than the spin-down limit considered above. Prior to this article these were the most sensitive studies made. Preliminary results for the same 28 pulsars using S3 data were given in Dupuis (2004) [14], and these are expanded below.

In addition to the above, data from the LIGO S2 run have been used to perform an all-sky (i.e., nontargeted) search for continuous wave signals from isolated sources, and a search for a signal from the neutron star within the binary system Sco-X1 [4]. An all-sky continuous wave search using the distributed computing project `Einstein@home`[2] has also been performed on S3 data [15]. These searches use the same search algorithms, are fully coherent and are ongoing using data from more recent (and therefore more sensitive) runs. Additional continuous wave searches using incoherent techniques are also being performed on LIGO data [16,17].

Unfortunately the pulsar population is such that most have spin frequencies that fall below the sensitivity band of current detectors. In the future, the low-frequency sensitivity of VIRGO [18] and Advanced LIGO [19] should allow studies of a significantly larger sample of pulsars.

C. The signal

Following convention, we model the observed phase evolution of a pulsar using a Taylor expansion about a fixed epoch time t_0:

$$\phi(T) = \phi_0 + 2\pi\{\nu_0(T - t_0) + \tfrac{1}{2}\dot{\nu}_0(T - t_0)^2 + \tfrac{1}{6}\ddot{\nu}_0(T - t_0)^3 + \ldots\}, \tag{1.3}$$

where ϕ_0 is the initial (epoch) spin phase, ν_0 and its time derivatives are the pulsar spin frequency and spin-down coefficients at t_0, and T is the pulsar proper time.

[1]The catalogue is continually updated and as such now contains more objects.

[2]http://einstein.phys.uwm.edu

The expected signal in an interferometer from a triaxial pulsar is

$$h(t) = \tfrac{1}{2}F_+(t;\psi)h_0(1+\cos^2\iota)\cos 2\phi(t) + F_\times(t;\psi)h_0\cos\iota\sin 2\phi(t), \quad (1.4)$$

where $\phi(t)$ is the phase evolution in the detector time t, F_+ and $F_\times$ are the detector antenna patterns for the plus and cross polarizations of gravitational waves, ψ is the wave polarization angle, and ι is the angle between the rotation axis of the pulsar and the line of sight. A gravitational wave impinging on the interferometer will be modulated by Doppler, time delay, and relativistic effects caused by the motions of the Earth and other bodies in the solar system. Therefore we need to transform the ''arrival time'' of a wave crest at the detector, t, to its arrival time at the solar system barycenter (SSB) t_b via

$$t_b = t + \delta t = t + \frac{\mathbf{r}\cdot\hat{\mathbf{n}}}{c} + \Delta_{E_\odot} + \Delta_{S_\odot}, \quad (1.5)$$

where $\mathbf{r}$ is the position of the detector with respect to the SSB, $\hat{\mathbf{n}}$ is the unit vector pointing to the pulsar, $\Delta_{E_\odot}$ is the special relativistic Einstein delay, and $\Delta_{S_\odot}$ is the general relativistic Shapiro delay [20]. Although pulsars can be assumed to have a large velocity with respect to the SSB, it is conventional to ignore this Doppler term and set $t_b = T$, as its proper motion is generally negligible (see Sec. VI A for cases where this assumption is not the case). For pulsars in binary systems, there will be additional time delays due to the binary orbit, discussed in Sec. III B.

II. INSTRUMENTAL PERFORMANCE IN S3/S4

The S3 and S4 runs used all three LIGO interferometers (H1 and H2 at the Hanford Observatory in Washington, and L1 at the Livingston Observatory in Louisiana) in the U.S. and the GEO 600 interferometer in Hannover, Germany. GEO 600 did not run for all of S3, but had two main data-taking periods between which improvements were made to its sensitivity. All these detectors had different duty factors and sensitivities.

A. LIGO

For S3 the H1 and H2 interferometers maintained relatively high duty factors of 69.3% and 63.4%, respectively. The L1 interferometer was badly affected by anthropogenic seismic noise sources during the day and thus had a duty factor of only 21.8%.

Between S3 and S4 the L1 interferometer was upgraded with better seismic isolation. This greatly reduced the amount of time the interferometer was thrown out of its operational state by anthropogenic noise, and allowed it to operate successfully during the day, with a duty factor of 74.5% and a longest lock stretch of 18.7 h. The H1 and H2 interferometers also both improved their duty factors to 80.5% and 81.4%, with longest lock stretches of almost a day.

The typical strain sensitivities of all the interferometers during S4 can be seen in Fig. 1. This shows the LIGO detectors reach their best sensitivities at about 150 Hz, while GEO 600 achieves its best sensitivity at its tuned frequency of 1 kHz.

B. GEO 600

During S3 GEO 600 was operated as a dual-recycled Michelson interferometer tuned to have greater sensitivity to signals around 1 kHz. The first period of GEO 600 participation in S3 was between 5 and 11 November 2003, called S3 I, during which the detector operated with a 95.1% duty factor. Afterwards, GEO 600 was taken offline to allow further commissioning work aimed at improving sensitivity and stability. Then from 30 December 2003 to 13 January 2004 GEO 600 rejoined S3, called S3 II, with an improved duty factor of 98.7% and with more than 1 order of magnitude improvement in peak sensitivity. During S3 there were five locks of longer than 24 hours and one lock longer than 95 hours. For more information about the performance of GEO 600 during S3 see Ref. [21].

GEO 600 participated in S4 from 22 February to 24 March 2005, with a duty factor of 96.6%. It was operated in essentially the same optical configuration as in S3. With respect to S3, the sensitivity was improved more than an order of magnitude over a wide frequency range, and close to 2 orders or magnitude around 100 Hz. For more information about GEO 600 during S4 see Ref. [22].

C. Data quality

When a detector is locked on resonance and all control loops are in their nominal running states and there are no

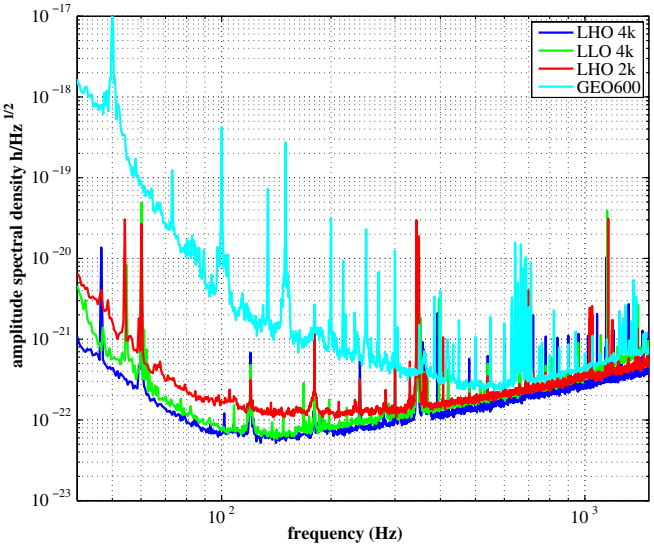

FIG. 1 (color online). Median strain amplitude spectral density curves for the LIGO and GEO 600 interferometers during the S4 run.

on-site work activities that are known to compromise the data, then the data are said to be *science mode*. All science mode data are not of sufficient quality to be analyzed however, and may be flagged for exclusion. Examples of such data quality flags are ones produced for epochs of excess seismic noise, and the flagging of data corrupted by overflows of photodiode analogue-to-digital converters. For this analysis we use all science mode data for which there is no corresponding data quality flag. For S3 this gives observation times of 45.5 days for H1, 42.1 days for H2, and 13.4 days for L1. For S4 this gives observation times of 19.4 days for H1, 22.5 days for H2, and 17.1 days for L1.

III. THE SEARCH METHOD

Our search method involves heterodyning the data using the phase model $\phi(t)$ to precisely unwind the phase evolution of the expected signal, and has been discussed in detail in Ref. [1]. After heterodyning, the data are low-pass filtered, using a ninth order Butterworth filter with a knee frequency of 0.5 Hz, and rebinned from the raw data sample rate of 16 384 Hz to 1/60 Hz, i.e., one sample per minute. The motion of the detector within the solar system modulates the signal and this is taken into account within the heterodyne by using a time delay given in Eq. (1.5), which transforms the signal to the SSB. Signals from binary pulsar systems contain an extra modulation term, as discussed briefly below, and these we targeted for the first time in S3/S4.

The search technique used here is currently only able to target emission at twice the pulsar's rotation frequency. Emission near the rotation frequency for a precessing star is likely to be offset from the observed pulsation frequency by some small factor dependent on unknown details of the stellar structure [7]. As our search technique requires precise knowledge of the phase evolution of the pulsar, such an additional parameter cannot currently be taken into account. For the emission at twice the rotation frequency there is no extra parameter dependence on the frequency and this is what our search was designed for.

We infer the pulsar signal parameters, denoted $\mathbf{a} = (h_0, \phi_0, \cos\iota, \psi)$, from their (Bayesian) posterior probability distribution function (pdf) over this parameter space, assuming Gaussian noise. The data are broken up into time segments over which the noise can be assumed stationary and we analytically marginalize over the unknown noise floor, giving a Student's t-likelihood for the parameters for each segment (see Ref. [1] for the method). Combining the segments gives an overall likelihood of

$$p(\{B_k\}|\mathbf{a}) \propto \prod_j^M \Bigg(\sum_{k=1+\sum_{i=1}^{j-1} m_i}^{\sum_{i=1}^{j} m_i} (\mathrm{Re}\{B_k\} - \mathrm{Re}\{y_k\})^2 + (\mathrm{Im}\{B_k\} - \mathrm{Im}\{y_k\})^2 \Bigg)^{-m_j}, \tag{3.1}$$

where each B_k is a heterodyned sample with a sample rate of one per minute, M is the number of segments into which the whole data set has been cut, m_j is the number of data points in the jth segment, and y_k, given by

$$y_k = \frac{1}{4} F_+(t_k;\psi) h_0 (1 + \cos^2\iota) e^{i2\phi_0} - \frac{i}{2} F_\times(t_k;\psi) h_0 \cos\iota e^{i2\phi_0}, \tag{3.2}$$

is the gravitational wave signal model evaluated at t_k, the time corresponding to the kth heterodyned sample. In Ref. [3] the value of m_j was fixed at 30 to give 30 minute data segments, and data that were contiguous only on shorter time scales, and which could not be fitted into one of these segments, were thrown out. In the analysis presented here, we have allowed segment lengths to vary from 5 to 30 minute, so we maximize the number of 30-minute segments while also allowing shorter segments at the end of locked stretches to contribute. The likelihood in Eq. (3.1) assumes that the data are stationary over each of these 30 minute (or smaller) segments. This assumption holds well for our data. Large outliers can also be identified and vetoed from the data, for example, those at the beginning of a data segment caused by the impulsive ringing of the low-pass filter applied after the data are heterodyned.

The prior probabilities for each of the parameters are taken as uniform over their respective ranges. Upper limits on h_0 are set by marginalizing the posterior over the nuisance parameters and then calculating the $h_0^{95\%}$ value that bounds the cumulative probability for the desired credible limit of 95%:

$$0.95 = \int_0^{h_0^{95\%}} p(h_0|\{B_k\}) \mathrm{d}h_0. \tag{3.3}$$

A. Combining data

In the search of Ref. [3] the combined data from the three LIGO interferometers were used to improve the sensitivity of the search. This was done by forming the joint likelihood from the three *independent* data sets:

$$p(B_k|\mathbf{a})_{\mathrm{Joint}} = p(B_k|\mathbf{a})_{\mathrm{H1}} \cdot p(B_k|\mathbf{a})_{\mathrm{H2}} \cdot p(B_k|\mathbf{a})_{\mathrm{L1}}. \tag{3.4}$$

This is valid provided the data acquisition is coherent between detectors, and supporting evidence for this is presented in Sec. V. It is of course a simple matter to extend Eq. (3.4) to include additional likelihood terms from other detectors, such as GEO 600.

In this analysis we also combine data sets from two different science runs. This is appropriate because S3 and S4 had comparable sensitivities over a large portion of the spectrum. Provided the data sets maintain phase coherence between runs, this combination can simply be achieved by concatenating the data sets from the two runs together for each detector.

An example of the posterior pdfs for the four unknown pulsar parameters of PSR J0024 − 7204C (each marginalized over the three other parameters) is shown in Fig. 2.

The pdfs in Fig. 2 are from the joint analysis of the three LIGO detectors using the S3 and S4 data, all combined coherently. The shaded area in the h_0 posterior shows the area containing 95% of the probability as given by Eq. (3.3). In this example the posterior on h_0 is peaked at $h_0 = 0$, though any distribution that is credibly close to zero is consistent with $h_0 = 0$. Indeed an upper limit can formally be set even when the bulk of the probability is well away from zero (see the discussion of hardware injections in Sec. V).

B. Binary models

Our previous known pulsar searches [2,3] have excluded pulsars within binary systems, despite the majority of pulsars within our detector band being in such systems. To address this, we have included an additional time delay to transform from the binary system barycenter (BSB) to pulsar proper time, which is a stationary reference frame with respect to the pulsar. The code for this is based on the widely used radio pulsar timing software TEMPO [23]. The algorithm and its testing are discussed more thoroughly in Ref. [24].

There are five principal parameters describing a Keplerian orbit: the time of periastron, T_0; the longitude of periastron, ω_0; the eccentricity, e; the period, P_b; and the projected semimajor axis, $x = a \sin i$. These describe the majority of orbits very well, although to fully describe the orbit of some pulsars requires additional relativistic parameters. The basic transformation and binary models

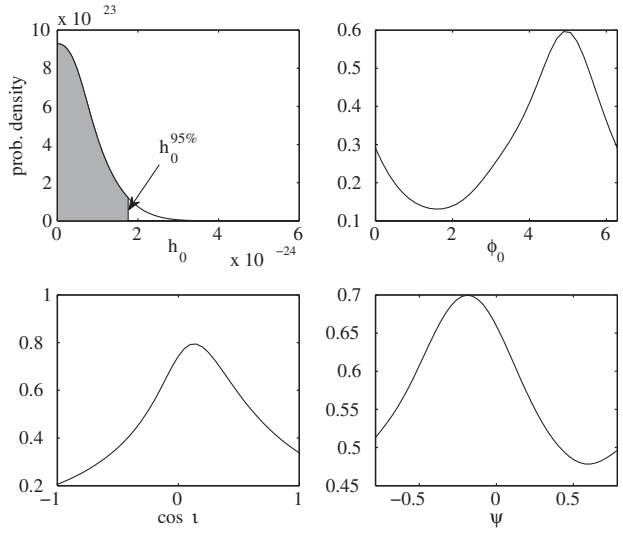

FIG. 2. The marginalized posterior pdfs for the four unknown pulsar parameters h_0, ϕ_0, $\cos\iota$, and ψ, for PSR J0024 − 7204C using the joint data from the three LIGO detectors over S3 and S4.

below are summarized by Taylor and Weisberg [20] and Lange *et al.* [25], and are those used in TEMPO. The transformation from SSB time t_b to pulsar proper time T follows the form of Eq. (1.5) and is

$$t_b = T + \Delta_R + \Delta_E + \Delta_S, \tag{3.5}$$

where Δ_R is the Roemer time delay giving the propagation time across the binary orbit, Δ_E is the Einstein delay which gives gravitational redshift and time dilation corrections, and Δ_S is the Shapiro delay which gives the general relativistic correction (see Ref. [20] for definitions of these delays).

The majority of binary pulsars can be described by three orbital models: the Blandford-Teukolsky (BT) model, the low eccentricity (ELL1) model, and the Damour-Deruelle (DD) model (see Refs. [20,23,25] for further details of these models). These different models make different assumptions about the system and/or are specialized to account for certain system features. For example, the ELL1 model is used in cases where the eccentricity is very small, and therefore periastron is very hard to define, in which case the time and longitude of periastron will be highly correlated and have to be reparametrized to the Laplace-Lagrange parameters [25]. When a binary pulsar's parameters are estimated from radio observations using TEMPO, the different models are used accordingly. These models can be used within our search to calculate all the associated time delays and therefore correct the signal to the pulsar proper time, provided we have accurate model parameters for the pulsar.

IV. PULSAR SELECTION

The noise floor of the LIGO detectors increases rapidly below about 50 Hz, so pulsar targets were primarily selected on their frequency. The choice of a 50 Hz gravitational wave frequency cutoff (pulsar spin frequency of 25 Hz) is somewhat arbitrary, but it also loosely reflects the split between the population of fast (millisecond/recycled and young) pulsars and slow pulsars.

All 154 pulsars with spin frequencies >25 Hz were taken from the ATNF online pulsar catalogue [13] (described in Ref. [26]). The accuracy of these parameters varies for each pulsar and is dependent on the time span, density of observations, and the noise level of the timing observations. Clearly it is important to ensure that parameter uncertainties do not lead to unacceptable phase errors in the heterodyne. Pulsars are not perfect clocks, so the epoch of the parameters is also important as more recent measurements will better reflect the current state of the pulsar. Importantly, there is near-continuous monitoring of the Crab pulsar at Jodrell Bank Observatory, and as such its parameters are continuously updated [27].

Precise knowledge of the phase evolution of each target pulsar is vital for our analysis, and possible effects that

may lead to a departure from the simple second-order Taylor expansion are discussed below.

A. Pulsar timing

Using TEMPO, we obtained the parameters of 75 pulsars from the regular observation programs carried out at Jodrell Bank Observatory and the Parkes Telescope (see Ref. [28] for details of the techniques used for this). For 37 of these the timings spanned the period of S3. These same model parameters were used to extrapolate the pulsar phases to the period of S4. The effect of parameter uncertainties on this extrapolation is discussed in Sec. IV B, but is only important in its effect on the extrapolated phase. For those pulsars observed during S3 the interpolation is taken to be free from significant error.

The parameters for 16 additional pulsars (for which new timings were not available) were taken directly from the ATNF catalogue, selected using criteria described in the following section. The parameters of the x-ray pulsar PSR J0537 − 6910 were taken from Ref. [29] and those for the Crab pulsar from the Jodrell Bank monthly ephemeris [27]. The remaining 61 pulsars (from the original list of 154) were not timed with sufficient confidence and were excluded from the search. This included many of the newly discovered pulsars (for example the 21 millisecond pulsars in the Terzan 5 globular cluster [30]) for which accurate timing solutions have yet to be published. We therefore had a catalogue of 93 timed pulsars for our gravitational wave search.

B. Error propagation in source parameters

The impact of parameter uncertainties on the search was assessed for both the S3 and S4 runs. At some level there are positional, frequency, and frequency derivative uncertainties for all the target pulsars, and for pulsars in a binary system there are also uncertainties associated with all the binary orbital parameters. Some of these uncertainties are correlated; for example, the error on frequency could affect the accuracy of the first frequency derivative, and the binary time of periastron and longitude of periastron are also highly correlated.

We took a "worst-case scenario" approach by adding and subtracting the quoted uncertainties from the best-fit values of all the parameters to determine the combination which gave a maximum phase deviation, when propagated over the period of the run (either S3 or S4), from the best-fit phase value calculated over the same time period. For example, if we assume $\phi(t_{\mathrm{S3}})$ given by Eq. (1.3) (ignoring, for simplicity, the ϕ_0 and $\ddot{\nu}$ terms) is the best-fit phase over the time span of S3, t_{S3}, the maximum phase uncertainty is

$$\Delta\phi_{\mathrm{err}} = \max[|\phi(t_{\mathrm{S3}}) \pm 2\pi\{(\nu \pm \sigma_\nu)(t_{\mathrm{S3}} \pm \sigma_{t_{\mathrm{S3}}} + \tfrac{1}{2}(\dot{\nu} \pm \sigma_{\dot{\nu}})(t_{\mathrm{S3}} \pm \sigma_{t_{\mathrm{S3}}})^2 + \ldots\}|], \quad (4.1)$$

where the σ's are the uncertainties on the individual parameters. Correlations between the parameters mean that this represents an upper limit to the maximum phase uncertainty, sometimes greatly overestimating its true value.

There are 12 pulsars with overall phase uncertainty $>30°$ in S3, which we take as the threshold of acceptability. A 30° phase drift could possibly give a factor of $\sim 1 - \cos 30° = 0.13$ in loss of sensitivity for a signal. Nine of these are in binary systems (PSRs J0024 − 7204H, J0407 + 1607, J0437 − 4715, J1420 − 5625, J1518 + 0205B, J1709 + 2313, J1732 − 5049, J1740 − 5340, and J1918 − 0642), and in five of these T_0 and ω_0 contribute most to the phase uncertainty. For the three isolated pulsars (PSRs J0030 + 0451, J0537 − 6910, and J1721 − 2457) the phase error is dominated by uncertainties in frequency and/or position.

Applying the same criterion to the time span of S4, we find that PSR J1730 − 2304 rises above the limit. For this pulsar its parameter uncertainties do not affect it for the S3 analysis as it was timed over this period; however when extrapolating over the time of the S4 run the uncertainties become non-negligible.

In total there are 13 pulsars rejected over the combined run. This highly conservative parameter check reduces our 93 candidate pulsars to 80.

C. Timing noise

Pulsars are generally very stable rotators, but there are phenomena which can cause deviations in this stability, generically known as timing noise. The existence of timing noise has been clear since the early days of pulsar astronomy and appears as a random walk in phase, frequency, or frequency derivative of the pulsar about the regular spin-down model given in Eq. (1.3) [31]. The strength of this effect was quantified in Ref. [31] as an *activity parameter* A, referenced to that of the Crab pulsar, and in Ref. [32] as a *stability parameter* Δ_8. A is based on the logarithm of the ratio of the rms residual phase of the pulsar, after removal of the timing model, to that of the Crab pulsar over an approximately three-year period. Δ_8 is not based on the stochastic nature of the Crab pulsar's timing noise and is defined for a fixed time (10^8 s) as

$$\Delta_8 = \log\left(\frac{1}{6\nu}|\ddot{\nu}| \times (10^8\ \mathrm{s})^3\right). \quad (4.2)$$

This assumes that the measured value of $\ddot{\nu}$ is dominated by the timing noise rather than the pulsar's intrinsic second spin-down derivative. Although generally true, this assumption is not valid for the Crab pulsar and PSR J0537 − 6910, where a nontiming noise dominated $\ddot{\nu}$ can be measured between glitches.[3] This quantity relates to the pulsar

[3]These two pulsars are among the most prolific glitchers, and in any global fit to their parameters the value of $\ddot{\nu}$ would most likely be swamped by the glitch events.

clock error caused by timing noise. The value of $\ddot{\nu}$ is so small as to be unmeasurable for most pulsars, although an upper limit can often be defined. Arzoumanian *et al.* [32] deduce, by eye, a linear relationship between Δ_8 and $\log\dot{P}$ of

$$\Delta_8 = 6.6 + 0.6\log\dot{P}, \tag{4.3}$$

where $\dot{P} = -\dot{\nu}/\nu^2$ is the period derivative.

As defined, Δ_8 is a somewhat imprecise indicator of the timing noise, not least because the time span of 10^8 seconds chosen by Arzoumanian *et al.* was simply the length of their data set. A preferred measure may simply be the magnitude and sign of $\ddot{P}$, but we shall continue to use the Δ_8 parameter as our timing noise magnitude estimate for the current analysis. A thorough study of timing noise, comparing and contrasting the various measures used, will be given in Ref. [33] (also see Refs. [28,34]).

There is a definite correlation between the Δ_8 parameters, spin-down rate, and age. Young pulsars, like the Crab pulsar, generally show the most timing noise. The categorization of the type of timing noise (i.e., phase, frequency, or frequency derivative) in Ref. [31] allowed them to ascribe different processes for each. The majority of pulsars studied showed frequency-type noise, possibly a result of random fluctuations in the star's moment of inertia. The actual mechanism behind the process is still unknown, with Cordes and Greenstein [35] positing and then ruling out several mechanisms inconsistent with observations.

Timing noise intrinsically linked to motions of the electromagnetic emission source or fluctuations in the magnetosphere, rather than the rotation of the pulsar, is important in the search for gravitational waves as it may allow the relative phase of the electromagnetic and gravitational signals to drift. The implications of timing noise in this context are discussed by Jones [36]. He gives three categories of timing noise, not necessarily related to the three types of timing noise given by Cordes and Helfand [31], having different effects on any search. If all parts of the neutron star are strongly coupled on short time scales, there should be no difference between the electromagnetic phase and the gravitational wave phase. If the timing noise were purely a magnetospheric fluctuation, then phase wandering caused by timing noise would not be seen in the gravitational wave emission. The third possibility, whereby the electromagnetic emission source wanders with respect to the mass quadrupole, could result from a weak exchange of angular momentum between the parts of the star responsible for electromagnetic and gravitational wave emission. Jones describes the ratio of the electromagnetic and gravitational timing noise phase residuals ($\Delta\Phi$) by a parameter $\alpha = \Delta\Phi_{\rm gw}/\Delta\Phi_{\rm em}$, with the three types of timing noise described above corresponding to $\alpha = 1$, 0 and $-I_{\rm em}/I_{\rm gw}$ respectively, where the I's represent the moments of inertia of the electromagnetic and gravitational wave producing components. In principle, this factor could be included as another search parameter. However, given the cost of including an extra parameter in this search, and given that it is plausible that all parts of a neutron star are tightly coupled on the time scales of interest here, we will assume rigid coupling between the two components, i.e. set $\alpha = 1$, corresponding to the gravitational and electromagnetic signals remaining perfectly in phase.

The Crab pulsar is regularly monitored [27] on time scales that are sufficiently short to allow its timing noise to be effectively removed using a second heterodyne procedure [37]. Like the Crab pulsar, PSR J0537 − 6910 is young, has a high glitch rate, and also shows high levels of timing noise [29]. Unfortunately, unlike the Crab pulsar, we have no regular ephemeris for it that covers our data set, and timing irregularities are likely to be too great for historical data to be of use. We therefore have excluded PSR J0537 − 6910 from the analysis. For less noisy pulsars we still need a method of estimating the effect of timing noise on phase evolution that does not rely on continuous observation. One such estimate is the Δ_8 parameter given by Eq. (4.2), which can provide a measure of the cumulative phase error. For those pulsars with a measured $\ddot{\nu}$ we use this estimate to obtain a corresponding value of Δ_8 as shown in Fig. 3.

This should provide a reasonable estimate of the timing noise over the time span of the pulsar observation. Again we apply our criterion that cumulative phase errors of $>30°$ are unacceptable. In Fig. 3 there are four pulsars (those with the four largest Δ_8 values), with measured $\ddot{\nu}$, for which this is the case, and therefore timing noise could be a problem (having already noted the Crab pulsar and

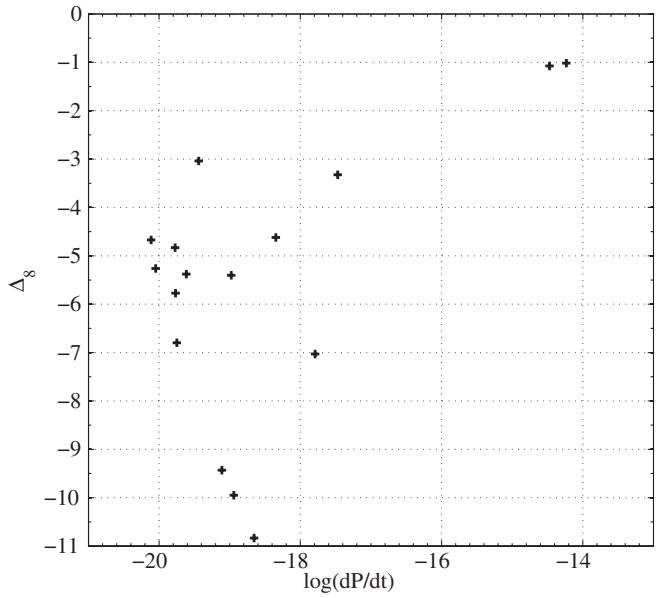

FIG. 3. The values of Δ_8 for our selection of pulsars with measured $\ddot{\nu}$.

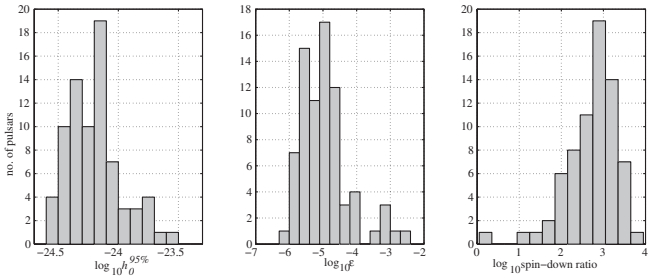

FIG. 4. Histograms of the log of amplitude, ellipticity, and ratio of spin-down to gravitational wave upper limits for the combined LIGO S3 and S4 run.

PSR J0537 − 6910 as exceptions): PSRs J1748 − 2446A, J1823 − 3021A, J1913 + 1011, and J1952 + 3252. For pulsars with no measured $\ddot{\nu}$ we use the approximate linear relation between the period derivative $\dot{P}$ and Δ_8 given in Eq. (4.3). The low $\dot{P}$ values for these pulsars imply that timing noise will be negligible.

In addition to the above, there are some pulsars in globular clusters for which there is no $\ddot{\nu}$ and for which $\dot{P}$ is negative ($\dot{\nu}$ is positive), so no value of Δ_8 can be assigned either through Eq. (4.2) or Eq. (4.3). For these pulsars the value of $\dot{\nu}$ (and therefore $\ddot{\nu}$) must be rather small to have been affected by motions within the cluster (discussed more in Sec. VI), so timing noise should again be negligible.

For pulsars which were retimed over the period of S3, timing noise will be negligible (for the S3 analysis at least), as any timing noise, which usually has variations on time scales of several months to years, will have been absorbed in the parameter estimation. PSRs J1748 − 2446A and J1823 − 3021A were retimed over S3, meaning that their S3 results will stand, although the other two will not. However, being conservative, we will remove all four pulsars with large values of Δ_8, and PSR J0537 − 6910, in which timing noise could be problematic, from the S4 and joint analysis. Note that PSR J0537 − 6910 is vetoed by both the parameter error criterion and our timing noise criterion.

This reduces our final number of well-parametrized pulsar targets to 78 for the S3 analysis and 76 for the S4 and joint analyses. The 76 pulsars include 21 of the 28 from the previous study of Abbott *et al.* [3], and so through our selection criterion we lose the following 7 previously analyzed pulsars: PSRs J0030 + 0451, J1721 − 2457, J1730 − 2304, J1823 − 3021A, J1910 − 5959B, J1913 + 1011, and J1952 + 3252. The same selection rules were not applied over S2; especially of note was that no timing noise criterion was considered, which accounts for three of the pulsars we lose between the two analyses. Also, our 30° rule was strictly applied, which the other four pulsars just exceeded.

The analysis was actually performed on all 93 timed pulsars mentioned above; however, the various parameter uncertainties preclude us setting upper limits on a total of 15 of these.

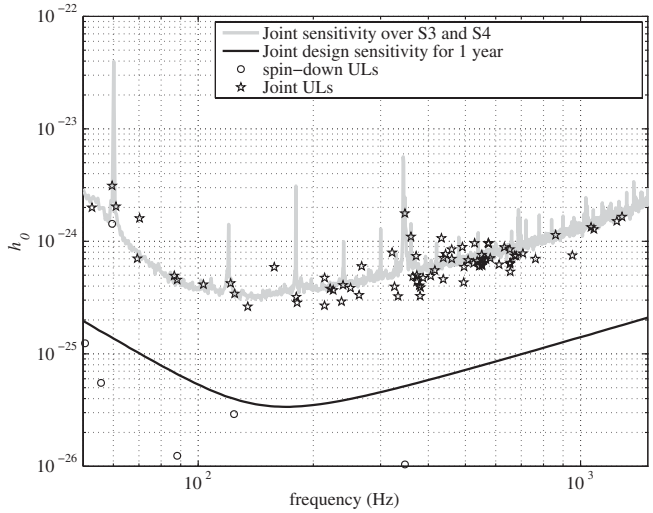

FIG. 5. The combined S3 and S4 upper limit results on the amplitude of gravitational waves for 76 pulsars using LIGO data compared to the joint sensitivity curve.

V. HARDWARE INJECTIONS

For analysis validation purposes, simulated gravitational wave signals for a variety of sources (bursts, pulsars, inspirals, and stochastic) have been mechanically injected into the LIGO interferometers during science runs. During S2 two pulsar signals were injected [3]. This was increased to 10 injections in the LIGO instruments for S3 and 12 for S4, covering a wider range of signal parameters. Extracting and understanding these injections has been invaluable in validating the analysis.

The hardware injection signals are produced using software (under LALAPPS [38]), which was largely developed independently of the extraction code. However, the codes do share the same solar system barycentering and detector antenna response function routines, both of which have been extensively checked against other sources (e.g. checks against TEMPO in Refs. [1,24]).

The signals were added into each of the three LIGO detectors via the position control signal going to the end test mass in one arm. Control signals in the digital servos that maintain optical cavities on resonance were summed with fake pulsar waveforms, modulating mirror positions to mimic the effect of a real spinning compact object (i.e. differential length motions with frequency and amplitude modulations appropriate for a given sky position, frequency, and spin-down). Furthermore, as the digital fake waveforms have to be converted to analog coil currents of suspended optics, the injected waveforms have to be divided by the transfer function of the output chain (predominantly the pendulum), in order to produce the desired differential length response of the cavity.

The extraction of these injections is described in detail in Appendix B. They show the relative phase consistency between the detectors over the course of a run. This means that a joint analysis combining the data from all detectors is valid. The injection plots (see Figs. 7 and 8) show what we would expect our posterior plots to look like given a detection, i.e. strongly peaked pdfs with very small probability at $h_0 = 0$, as compared to those in Fig. 2 where h_0 peaks at zero.

VI. RESULTS

A. Upper limits

Here we present 95% degree-of-belief upper limits on the amplitude of gravitational waves (h_0) from the 78 pulsars identified above. The value of h_0 is independent of any assumptions about the neutron star other than it is emitting gravitational waves at twice its rotation frequency. The results will also be presented in terms of the pulsars' equatorial ellipticity ε, which under the assumption of triaxiality is related to h_0 via Eq. (1.1) by

$$\varepsilon = 0.237\left(\frac{h_0}{10^{-24}}\right)\left(\frac{r}{1\ \mathrm{kpc}}\right)\left(\frac{1\ \mathrm{Hz}}{\nu}\right)^2\left(\frac{10^{38}\ \mathrm{kg\,m^2}}{I_{zz}}\right). \quad (6.1)$$

To obtain an upper limit on ε from that for h_0, we assume a fiducial moment of inertia value of $I_{zz} = 10^{38}\ \mathrm{kg\,m^2}$. We discuss below in Sec. VI B the effect of relaxing this assumption. Pulsar distances are taken from the ATNF catalogue [13] and are generally derived from the radio dispersion measures, with errors estimated to be of order 20%, although in some cases even this can be an underestimate. A critical review of pulsar distance measurements can be found in Ref. [39].

All upper limit results from the individual S3 and S4 runs along with results from the combined run, with and without GEO 600 included, are given in Appendix A in Tables III and IV. The GEO 600 data only provides comparable sensitivities to LIGO at frequencies greater than 1000 Hz, and are therefore only used in the search for PSR J1939 + 2134 (at the time, the fastest known millisecond pulsar) in S3, and additionally PSR J1843 − 1113 in S4 and the combined run. Inclusion of GEO 600 does not significantly change the joint upper limits for these pulsars. For the majority of pulsars the lowest upper limits come from the combined S3/S4 data set, although for 14 pulsars (PSRs J0024 − 7204I, J0024 − 7204S, J0024 − 7204U, J0621 + 1002, J1045 − 4509, J1757 − 5322 J1802 − 2124, J1804 − 2717, J1857 + 0943, J1910 − 5959D, J1910 − 5959E, J1911 + 0101B, J2129 − 5721, and J2317 + 1439) the S4 results alone provide a lower limit. The combined S3 and S4 run results are presented in histogram form in Fig. 4.

Figure 5 shows the results compared to a joint LIGO S4 upper limit estimate curve, taken as the best sensitivity during S4.

The joint upper limit sensitivity curve for the three detectors can be estimated by combining the detector one-sided power spectral densities (PSDs) via

$$S(f) = \left(\frac{T_{\mathrm{obs\,H1}}}{S_h(f)_{\mathrm{H1}}} + \frac{T_{\mathrm{obs\,H2}}}{S_h(f)_{\mathrm{H2}}} + \frac{T_{\mathrm{obs\,L1}}}{S_h(f)_{\mathrm{L1}}}\right)^{-1},$$
$$h_0^{95\%} = 10.8\sqrt{S(f)}, \quad (6.2)$$

where $S_h(f)$ is the PSD and T_{obs} is each detector's live time (using the associated duty factor of each interferometer during the run). The factor of 10.8 is given in Ref. [1] and was calculated through simulations with Gaussian noise.[4]

The results are also compared to the upper limit deduced from the observed spin-down via Eq. (1.2), making the assumption that all rotational energy is lost through gravitational wave emission. The spin-down limit is seen as a natural crossing point after which gravitational wave data, including upper limits, have a likely bearing on the nature of the neutron star. The spin-down upper limit will obviously depend on $\dot{\nu}$. This value, however, can be masked by radial and transverse motions of the object (see Ref. [40] for discussion of these effects). The Shklovskii effect [41], in which the pulsar has a large transverse velocity v, will cause an apparent rate of change in the pulsar's period of

$$\dot{P}_{\mathrm{S}} = \frac{v^2}{rc}P. \quad (6.3)$$

Its $1/r$ dependence makes this effect more prominent for nearby pulsars. In the ATNF catalogue [13] values of the intrinsic period derivative $\dot{P}_{\mathrm{int}} = \dot{P} - \dot{P}_{\mathrm{S}}$ can be obtained where this effect has been corrected for. This provides a measure of intrinsic (rather than apparent) spin-down[5] and, when available, is used in the spin-down ratio results.

The observed value of $\dot{P}_{\mathrm{obs}}$ will also differ from its intrinsic value, $\dot{P}_{\mathrm{int}}$, if the pulsar is accelerating—a likely scenario in the gravitational field of a globular cluster [40]. Any line-of-sight component to the acceleration, $a_{\parallel}$, will give an observed value of

$$\dot{P}_{\mathrm{obs}} = \dot{P}_{\mathrm{int}} + \frac{a_{\parallel}}{c}P \quad (6.4)$$

where P is the spin period [42]. These effects can cause pulsars to have apparent spin-ups (seen in quite a large number of globular cluster pulsars), although they are only strong enough to greatly affect pulsars with intrinsically small period derivatives. There are still many globular clusters for which the radial accelerations have not been

[4] In Ref. [3] a similar plot to Fig. 5 is shown for the S2 data using a factor of 11.4 in the relation between the upper limit and PSD. This definition comes from using the $\mathcal{F}$-statistic search method and setting a 1% false alarm rate and 10% false dismissal rate for signals given the underlying detector PSD [2]

[5] Note that the heterodyne procedure still needs to make use of the measured spin-down rather than the intrinsic spin-down, as these Doppler effects will have the same effect on the gravitational waves.

measured; therefore no firm spin-down upper limit can be set, making the direct gravitational wave results a unique limit.

Highlights of the combined S3/S4 results include the tightest strain upper limit set on a pulsar of $h_0^{95\%} = 2.6 \times 10^{-25}$ for PSR J1603 − 7207, the smallest ellipticity at $\varepsilon = 7.1 \times 10^{-7}$ for PSR J2124 − 3358, and the closest upper limit to the spin-down limit at a ratio of 2.2 for the Crab pulsar (PSR J0534 + 2200).

B. Dependence on the moment of inertia

The pulsar ellipticity results detailed above assume a moment of inertia of 10^{38} kg m^2, which is the standard fiducial number used in the literature. However, modern theoretically computed equations of state (EOS) generally predict somewhat larger moments of inertia for stars more massive than $1M_\odot$, a group which includes all neutron stars with measured masses (see Ref. [43]). Therefore the dependence on the moment of inertia should be considered.

Bejger, Bulik, and Haensel [44] give an overview of the theoretical expectations for the moment of inertia. Their Fig. 2 plots the moment of inertia vs mass for several theoretically predicted types of EOS. The maximum moment of inertia they find (after varying the mass of the star) is 2.3 times the fiducial value, with stars of $1.4M_\odot$ having moments of inertia 1.2–2.0 except for one outlying type of EOS. Typically the maximum moment of inertia occurs for a neutron star mass of $1.7M_\odot$ or more. Recently masses greater than 1.6–$1.7M_\odot$ with 95% confidence have been measured [30,45] for some systems, making this reasonable to consider. More recently Lackey [46] found the highest moment of inertia to be 3.3×10^{38} kg m^2 for EOS G4 of Lackey, Nayyar, and Owen [47]. This is a relativistic mean-field EOS similar to the Glendenning nucleon-hyperon model family considered by Bejger, Bulik, and Haensel [44] but contains no exotic phases of matter such as hyperons or quarks. Consequently, we consider the range of theoretically predicted moments of inertia to be approximately 1–3 $\times 10^{38}$ kg m^2.

There have been recent attempts to infer neutron star moments of inertia from observations. Bejger and Haensel [48,49] derived a value for the Crab pulsar's moment of inertia by equating the spin-down power to the observed electromagnetic luminosity and inferred acceleration of the nebula. However, this (extremely high) value is dominated by the assumptions about the highly uncertain mass and mass distribution of the nebula as well as the relativistic wind from the pulsar, and thus cannot yet be considered to give a reliable value. The double pulsar system J0737 − 3039 shows great promise for tighter measurements of the moment of inertia (and constraints on the EOS) in the near future [44,50–52]. However, for the moment, we are left with the theoretical range quoted above.

As suggested in Ref. [53], instead of using Eq. (6.1) to set a limit on ε assuming a value of I_{zz}, one can use it to set a limit on the neutron star quadrupole moment $\approx I_{zz}\varepsilon$ without relying on any assumption about I_{zz}. The limit on the quadrupole moment can then be used to help define an exclusion region in the I-ε plane. This exclusion region allows one to read off an upper limit on ε as a function of the EOS-dependent moment of inertia. The spin-down can also be used to provide exclusion regions via the relation

$$I_{zz} = \frac{5}{512\pi^4} \frac{|\dot{\nu}|c^5}{G\nu^5} \frac{1}{\varepsilon^2}. \tag{6.5}$$

Theoretical contributions to the exclusion regions come from predictions of the maximum moment of inertia and ellipticity. In terms of the exclusion region, our observational upper limits on h_0 are far from contributing except for the Crab pulsar, to which we now turn.

C. The Crab pulsar—PSR J0534 + 2200

Of the known radio pulsars, the Crab pulsar has often been considered one of the most promising sources of gravitational waves. This is due to its youth and large spin-down rate, leading to a relatively large spin-down upper limit several orders of magnitude higher than for most other pulsars. The high rate of glitching in the pulsar also provides possible evidence of asymmetry. One glitch model favored for the Crab pulsar involves a change in the pulsar ellipticity, and breaking of the crust, as the star settles to its new equilibrium state as it spins down [40]. In the 1970s, estimates of gravitational wave strains were spurred on by the experimenters producing novel technologies which allowed the possibility of probing these low strains, with Zimmermann [54] producing estimates of gravitational wave strains from the Crab pulsar ranging from $h_0 \approx 2 \times 10^{-25}$–$10^{-29}$.

The first searches for gravitational waves from the Crab pulsar were carried out using specially designed resonant bar detectors, with frequencies of around 60 Hz [9]. The most recent result using such a bar was from 1993 and gave a 1σ upper limit of $h_0 \leq 2 \times 10^{-22}$ [10]. This upper limit was passed in the LIGO S2 run, which gave $h_0^{95\%} = 4.1 \times 10^{-23}$ [3]. Using Eq. (1.2), and taking $I_{zz} = 10^{38}$ kg m^2 and $r = 2$ kpc, gives a spin-down upper limit for the Crab pulsar of $h_0 < 1.4 \times 10^{-24}$, about a factor of 30 below the S2 observational upper limit. However, the S2 limit on the Crab was, at the time, the closest approach to the spin-down limit obtained for any pulsar.

Our new results for the Crab pulsar (and the other 77 targets) are shown in Table III. The results improve by up to an order of magnitude over those from the S2 run, and the majority of this improvement was between the S2 and S3 runs. The results for the Crab pulsar over the S2, S3, and S4 runs are plotted on the I-ε plane in Fig. 6.

The solid lines in Fig. 6 mark the lower boundaries of exclusion regions on this plane using our upper limits obtained for the different runs. The dashed black diagonal line marks the lower boundary of the upper limit from spin-

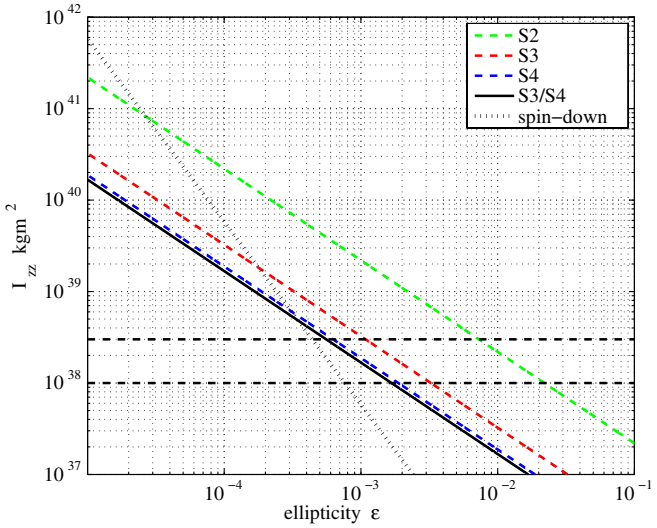

FIG. 6 (color online). The moment of inertia–ellipticity plane for the Crab pulsar over the S2, S3, and S4 runs. The areas to the right of the diagonal lines are the experimentally excluded regions. The horizontal lines represent theoretical upper and lower limits on the moment of inertia as mentioned in Sec. VI B. Theoretical upper limits on the ellipticity are much more uncertain, the highest being a few times 10^{-4}.

down as given in Eq. (6.5). The dashed horizontal black lines give lower and upper bounds on the moment of inertia of $1–3 \times 10^{38}$ kg m^2, as given by our arguments in Sec. VI B. It can be seen that our experimental results currently only beat the spin-down limit for moments of inertia at values greater than almost double the maximum of our theoretical range. However, over this range the ratio of the gravitational to spin-down upper limit ranges from 2.2 at the lowest value to only 1.3 at the largest value.

The spin-down limit, in fact, overestimates the strongest possible signal because we know that much of the spin-down energy of the Crab goes into powering the nebula through electromagnetic radiation and relativistic particle winds. Thus it is interesting to ask how far we would need to beat the spin-down limit by to have a chance of detecting a signal allowing for what is known about the nongravitational wave spin-down. Palomba [55] uses the observed braking index 2.51 of the Crab pulsar with a simple model of spin-down through gravitational radiation (braking index 5) combined with some other mechanism (braking index a free parameter) to place an upper limit of about $\varepsilon \leq 3 \times 10^{-4}$. This is about 2.5 times lower than the spin-down limit and 5.5 times lower than our result (for $I_{zz} = 10^{38}$ kg m^2).

The Crab pulsar experienced two glitches between S3 and S4, a large glitch on 6 September 2004 and a smaller glitch on 22 November 2004 [27]. The effect of glitches on the relative phase between the electromagnetic pulse and any possible gravitational wave signal is unknown, so there is uncertainty whether the (phase-coherent) combined S3/S4 result is valid. The combined result stands, but the reader should be aware that it includes the assumption of trans-glitch phase coherence.

VII. ASTROPHYSICAL INTERPRETATION

We have produced new, tight, upper limits on gravitational wave signal strength from a large selection of known pulsars, and for the Crab pulsar we are very near the fiducial limit set by spin-down arguments.

It can be seen from Table III and Fig. 4 that, for the majority of pulsars, the gravitational wave detector upper limits are at least 100 times above those from the spin-down argument, so is there anything that we can take from the results in terms of astrophysics?

First, we should note that spin-down limits on gravitational wave luminosity are plausible, but model dependent. They assume a model for the structure of the neutron star (for instance, that it is not accreting and is rigidly rotating, in addition to assumptions about its equation of state), and they take dispersion measure distance as a consistently good measure of true distance. There is some considerable uncertainty associated with all of these assumptions. In contrast, our observations set direct limits on a source's gravitational wave strain.

Second, for globular cluster pulsars the spin-down measured from radio timing observations is a combination of the spin-down intrinsic to the pulsar and acceleration along the line of sight $a_\parallel$ in the cluster's gravitational potential [see Eq. (6.4)]. In general, the magnitude and sign of the acceleration is unknown but the intrinsic $\dot{P}_{\rm int} > 0$ of millisecond pulsars is usually small and often smaller than the extrinsic contribution. Only if $\dot{P}_{\rm obs} < 0$ can one be sure that $a_\parallel < 0$. Therefore, the limits derived from our gravitational wave observations provide the only direct limits on $\dot{P}_{\rm int}$ which are independent from biasing kinematic effects. These can be combined with the observed spin-down to provide a limit on the acceleration in the cluster, i.e. $a_\parallel \geq c(\dot{P}_{\rm obs} - \dot{P}_{\rm gw}^{\rm limit})/P$.

Finally, it is interesting to note that our ellipticity limits are well into the range permitted by some models of strange quark stars or hybrid stars ($\varepsilon \sim$ a few times 10^{-4}–10^{-5}) and are reaching into the range permitted by more conventional neutron star EOSs ($\varepsilon \sim$ a few times 10^{-7}) [56].

Currently the fifth LSC science run (S5) is underway, and this promises to beat the Crab pulsar spin-down limit within a few months of its start. For many other pulsars we should be able to reach amplitude upper limits of $<1 \times 10^{-25}$ and ellipticities of $\sim 1 \times 10^{-7}$.

ACKNOWLEDGMENTS

The authors gratefully acknowledge the support of the U.S. National Science Foundation for the construction and operation of the LIGO Laboratory, and the Particle Physics and Astronomy Research Council of the United Kingdom,

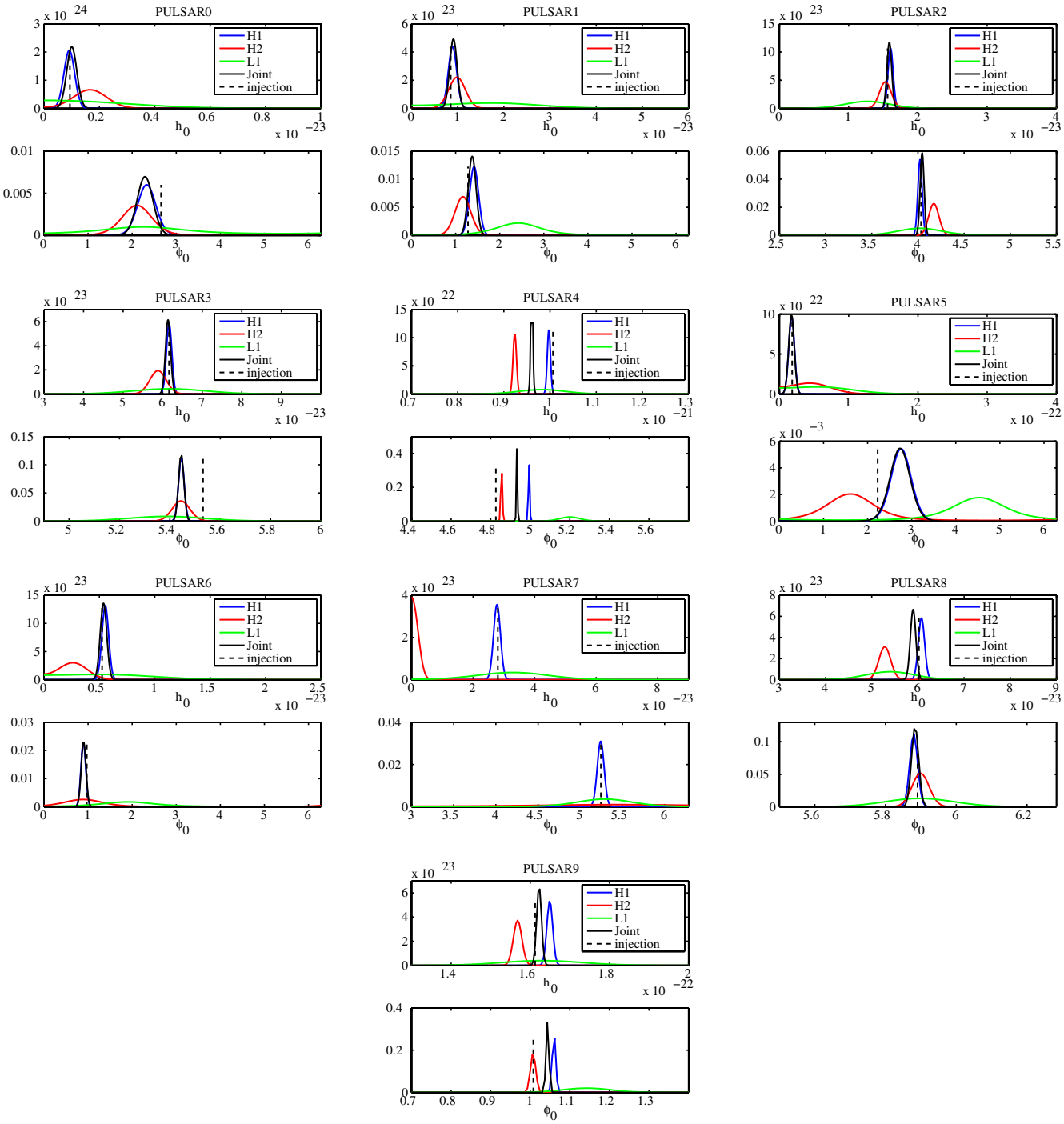

FIG. 7 (color online). The pdfs of h_0 and ϕ_0 for 10 isolated pulsar injections into the LIGO detectors during S3. The anomaly seen in PULSAR7 is discussed in the text.

the Max-Planck-Society, and the State of Niedersachsen/ Germany for support of the construction and operation of the GEO600 detector. The authors also gratefully acknowledge the support of the research by these agencies and by the Australian Research Council, the Natural Sciences and Engineering Research Council of Canada, the Council of Scientific and Industrial Research of India, the Department of Science and Technology of India, the Spanish Ministerio de Educacion y Ciencia, the National Aeronautics and Space Administration, the John Simon Guggenheim Foundation, the Alexander von Humboldt Foundation, the Leverhulme Trust, the David and Lucile Packard Foundation, the Research Corporation, and the Alfred P. Sloan Foundation.

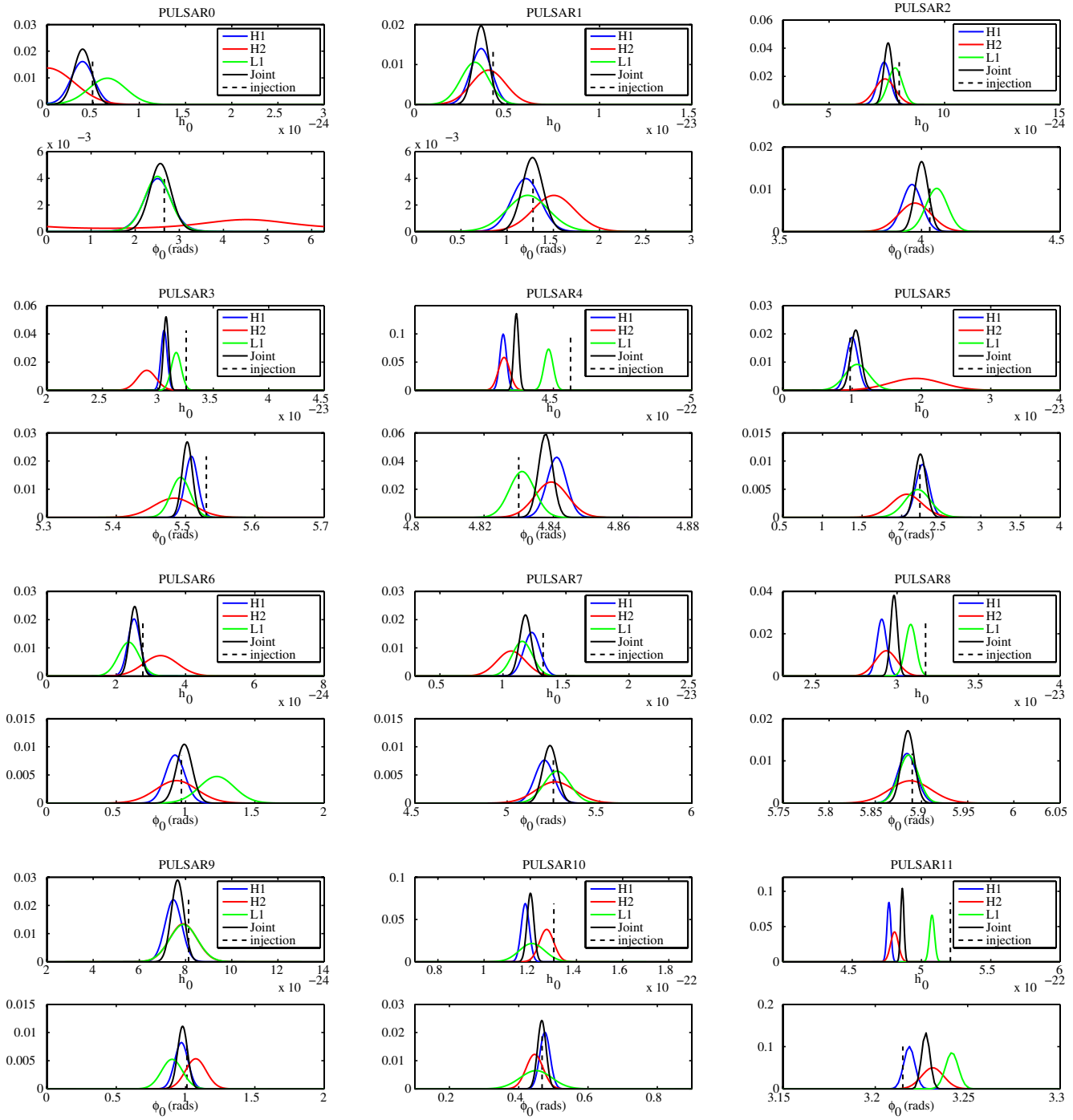

FIG. 8 (color online). The pdfs of h_0 and ϕ_0 for 10 isolated and 2 binary pulsar injections into the LIGO detectors during S4.

APPENDIX A: TABLES OF UPPER LIMIT RESULTS

In Table III we present the upper limit results of the S3, S4, and combined S3 and S4 analyses for 78 pulsars using the LIGO interferometers. Table IV shows the upper limits including GEO 600 for the two fastest pulsars in the analysis. The upper limits are given in terms of the gravitational wave amplitude, pulsar ellipticity, and where applicable, the ratio of our direct limit to that given by spin-down arguments.

APPENDIX B: INJECTIONS

1. S3 injections

An initial analysis of the S3 pulsar injections is given in Ref. [14]. The data have since been reanalyzed with more recent versions of the detector calibrations, the results of

TABLE I. The parameter values for the pulsar hardware injections in S3 and S4.

PULSAR	α (rads)	δ (rads)	ν_{gw} (Hz)	$\dot{\nu}_{gw}$ (Hz/s)	h_0 (S3)	h_0 (S4)	ϕ_0 (rads)	ι (rads)	ψ (rads)
0	1.25	−0.98	265.5	-4.15×10^{-12}	9.38×10^{-25}	4.93×10^{-25}	2.66	0.65	0.77
1	0.65	−0.51	849.1	-3.00×10^{-10}	8.49×10^{-24}	4.24×10^{-24}	1.28	1.09	0.36
2	3.76	0.06	575.2	-1.37×10^{-13}	1.56×10^{-23}	8.04×10^{-24}	4.03	2.76	−0.22
3	3.11	−0.58	108.9	-1.46×10^{-17}	6.16×10^{-23}	3.26×10^{-23}	5.53	1.65	0.44
4	4.89	−0.21	1430.2	-2.54×10^{-8}	1.01×10^{-21}	4.56×10^{-22}	4.83	1.29	−0.65
5	5.28	−1.46	52.8	-4.03×10^{-18}	1.83×10^{-23}	9.70×10^{-24}	2.23	1.09	−0.36
6	6.26	−1.14	148.7	-6.73×10^{-9}	5.24×10^{-24}	2.77×10^{-24}	0.97	1.73	0.47
7	3.90	−0.36	1221.0	-1.12×10^{-9}	2.81×10^{-23}	1.32×10^{-23}	5.24	0.71	0.51
8	6.13	−0.58	194.3	-8.65×10^{-9}	6.02×10^{-23}	3.18×10^{-23}	5.89	1.50	0.17
9	3.47	1.32	763.8	-1.45×10^{-17}	1.61×10^{-22}	8.13×10^{-24}	1.01	2.23	−0.01
GEO	0.78	−0.62	1125.6	-2.87×10^{-11}	7.5×10^{-22}	*	1.99	0.84	0.37

which are presented here. For S3, initially 10 pulsar signals were injected, with a further one added at the end of the run to be in coincidence with a single injection into GEO 600 [57]. The majority of injection parameters were decided upon randomly, although pulsar frequencies were chosen to avoid major instrumental or calibration lines, and amplitudes were dependent on the frequency. The injections were split into two groups of five, where values of h_0 were calculated to give two each with signal-to-noise ratios of approximately 3, 9, 27, 81, and 243. The parameter values are shown in Table I.

The 10 initial signals were injected into the LIGO detectors for approximately the first half of the run, then turned off for two weeks, to ensure data were present that were not artificially contaminated, and then turned back on with the two loudest signals removed. The simultaneous injection with GEO 600 was switched on near the end of the run.

These signals were extracted from the data using the analysis techniques described in Sec. III and Ref. [1]. The two most important parameters for checking that the calibration of the instruments was correct were the amplitude and initial phase, so in the Bayesian parameter estimation procedure the ι and ψ parameters were held fixed at their known values. This was done because the correlations between h_0 and $\cos\iota$ and ϕ_0 and ψ, respectively, could lead to the marginalized posterior pdfs for each parameter being distorted or spread out (see Ref. [14] for examples of this). The extracted pdfs of h_0 and ϕ_0 for each of the injections, after corrections described below, can be seen in Fig. 7.

For the vast majority of signals the extracted pdfs overlap with the injected value. For the strongest injections with the largest signal-to-noise ratios the pdfs are rather narrow, and any uncertainties in the calibration become evident, with a maximum offset of the order of 10%–15%. The far wider pdfs associated with the L1 signal injections reflect the lower L1 sensitivity and lower duty factor compared with the H1 and H2 detectors. It can be seen that the injected phases for each detector agree with each other to within a few degrees and are within the uncertainty of the method. This provides some evidence that there is phase coherence between the detectors and that a joint analysis, combining the data from all the detectors, is possible.

Two main discrepancies have been identified as operational mistakes made during the injection procedure: PULSAR7 was injected into H2 with a much lower amplitude than intended, and remained undetected, and therefore no joint analysis was performed; and PULSAR0 was injected into H1 with an amplitude 1.6 times larger than intended.

The injection of the signal into GEO 600 is described in Ref. [57], and its analysis is described in Ref. [14]. It was found that the injection performed during S3 was badly contaminated and could not be used. However, a subsequent injection performed shortly after S3 has verified that the signal parameters were correctly injected and extracted, validating the injection hardware and analysis software.

2. S4 injections

The 10 injections used in S3 were used again for S4 to create artificial signals in the LIGO interferometers. However, their amplitudes were adjusted to give approximately the same signal-to-noise ratios as seen in S3, taking

TABLE II. The parameter values for the S4 binary pulsar hardware injections.

PULSAR	ν_{gw} (Hz)	h_0	T_0 (MJD)	P_b (days)	e	ω_0 (deg)	$a \sin i$ (sec)
10	250.6	1.30×10^{-22}	51 749.711 564 82	1.354 059 39	0.0	0.0	1.652 84
11	188.0	5.21×10^{-22}	52 812.920 411 76	0.319 633 90	0.180 567	322.571	2.7564

TABLE III. Pulsar upper limits using LIGO data from the S3 and S4 runs. The approximate pulsar spin frequencies and spin-down rates are given. A "*" denotes globular cluster pulsars for which no spin-down upper limit could be set. The values marked with a † represent pulsars for which the spin-down limit has been corrected for the Shklovskii effect. The ratio column gives the ratio of our experimental upper limits to the spin-down upper limits.

			S3						S4						S3 and S4					
			$\log h_0^{95\%}$				$\log\varepsilon$	Ratio	$\log h_0^{95\%}$				$\log\varepsilon$	Ratio	$\log h_0^{95\%}$				$\log\varepsilon$	Ratio
PULSAR	ν (Hz)	$\dot{\nu}$ (Hz s^{-1})	H1	H2	L1	Joint			H1	H2	L1	Joint			H1	H2	L1	Joint		
J0024 − 7204C	173.71	$+1.50 \times 10^{-15}$	−23.30	−23.55	−23.04	−23.64	−4.06	*	−23.08	−23.53	−23.31	−23.53	−3.96	*	−23.41	−23.69	−23.34	−23.75	−4.18	*
J0024−7204D	186.65	$+1.20 \times 10^{-16}$	−23.69	−23.72	−23.24	−23.82	−4.31	*	−23.97	−23.92	−23.95	−24.14	−4.63	*	−24.15	−23.99	−23.91	−24.36	−4.85	*
J0024−7204E	282.78	-7.88×10^{-15}	−23.90	−23.53	−23.19	−23.92	−4.76	1380†	−24.02	−23.93	−23.83	−24.15	−4.99	815†	−24.06	−24.03	−23.84	−24.16	−5.01	786†
J0024−7204F	381.16	-9.37×10^{-15}	−23.64	−23.47	−22.98	−23.70	−4.81	2403†	−23.91	−23.63	−23.53	−23.99	−5.10	1237†	−24.05	−23.63	−23.51	−24.16	−5.26	845†
J0024−7204G	247.50	$+2.58 \times 10^{-15}$	−24.05	−23.66	−23.14	−24.12	−4.85	*	−24.09	−23.99	−23.87	−24.29	−5.02	*	−24.16	−24.04	−23.88	−24.37	−5.10	*
J0024−7204I	286.94	$+3.78 \times 10^{-15}$	−23.74	−23.36	−23.13	−23.81	−4.67	*	−24.05	−23.96	−23.53	−24.04	−4.90	*	−23.97	−23.97	−23.56	−24.02	−4.88	*
J0024−7204J	476.05	$+2.22 \times 10^{-15}$	−23.65	−23.10	−22.86	−23.63	−4.93	*	−23.86	−23.78	−23.34	−24.06	−5.36	*	−23.89	−23.76	−23.34	−24.13	−5.43	*
J0024−7204L	230.09	$+6.46 \times 10^{-15}$	−23.99	−23.56	−23.25	−24.02	−4.69	*	−23.96	−23.96	−23.78	−23.97	−4.64	*	−24.12	−24.02	−23.78	−24.07	−4.74	*
J0024−7204M	271.99	$+2.84 \times 10^{-15}$	−23.93	−23.52	−23.00	−23.93	−4.75	*	−24.05	−24.01	−23.87	−24.20	−5.01	*	−24.06	−24.09	−23.81	−24.22	−5.03	*
J0024−7204N	327.44	$+2.34 \times 10^{-15}$	−23.81	−23.43	−23.11	−23.82	−4.79	*	−23.80	−23.76	−23.72	−24.13	−5.10	*	−24.00	−23.91	−23.70	−24.27	−5.25	*
J0024−7204Q	247.94	-2.09×10^{-15}	−23.94	−23.47	−23.29	−24.07	−4.81	1734	−24.06	−24.01	−23.65	−24.09	−4.82	1669	−24.14	−24.06	−23.66	−24.23	−4.96	1215
J0024−7204S	353.31	$+1.50 \times 10^{-14}$	−23.58	−23.35	−23.10	−23.60	−4.64	*	−23.97	−23.89	−23.62	−24.17	−5.21	*	−23.97	−23.97	−23.62	−24.11	−5.15	*
J0024−7204T	131.78	-5.10×10^{-15}	−24.17	−23.74	−23.47	−24.21	−4.39	591	−24.26	−24.19	−24.15	−24.45	−4.63	340	−24.29	−24.22	−24.17	−24.48	−4.66	319
J0024−7204U	230.26	-5.05×10^{-15}	−23.73	−23.64	−23.29	−23.83	−4.50	1886†	−24.01	−24.04	−23.68	−24.27	−4.94	693†	−23.94	−24.10	−23.70	−24.16	−4.83	900†
J0034−0534	532.71	-1.41×10^{-15}	−23.20	−23.20	−22.69	−23.45	−5.54	2653	−23.38	−23.36	−23.45	−23.81	−5.89	1171	−23.51	−23.43	−23.43	−23.87	−5.96	999
J0218 + 4232	430.46	-1.43×10^{-14}	−23.56	−23.41	−22.93	−23.66	−4.79	2740	−23.85	−23.49	−23.54	−23.84	−4.97	1821	−23.95	−23.59	−23.58	−23.94	−5.07	1430
J0534 + 2200	29.80	-3.73×10^{-10}	−23.18	−22.04	−22.40	−23.22	−2.49	4.23†	−23.42	−23.19	−22.96	−23.46	−2.73	2.45†	−23.49	−23.19	−22.96	−23.51	−2.78	2.18†
J0613−0200	326.60	-1.02×10^{-15}	−23.77	−23.33	−23.07	−23.80	−5.11	2571†	−23.72	−23.82	−23.73	−24.00	−5.32	1597†	−23.96	−23.86	−23.73	−24.07	−5.39	1365†
J0621 + 1002	34.66	-5.68×10^{-17}	−23.55	−22.56	−23.04	−23.60	−3.03	4675†	−23.83	−23.34	−23.95	−24.17	−3.61	1241†	−23.89	−23.34	−23.96	−24.15	−3.59	1301†
J0711−6830	182.11	-4.94×10^{-16}	−23.95	−23.21	−23.23	−24.01	−5.14	1018†	−24.10	−23.99	−23.88	−24.16	−5.29	733†	−24.25	−24.07	−23.85	−24.31	−5.44	513†
J0737−3039A	44.05	-3.38×10^{-15}	−24.05	−23.20	−23.28	−24.03	−4.19	75	−24.13	−23.80	−24.08	−24.28	−4.44	42	−24.27	−23.83	−24.08	−24.34	−4.50	37
J0751 + 1807	287.46	-6.43×10^{-16}	−23.87	−23.51	−23.22	−23.94	−5.69	604†	−23.78	−23.80	−23.66	−23.95	−5.70	590†	−23.91	−23.87	−23.63	−24.02	−5.77	496†
J1012 + 5307	190.27	-6.20×10^{-16}	−24.08	−23.75	−23.23	−24.06	−5.53	357†	−24.22	−24.03	−23.89	−24.42	−5.89	156†	−24.32	−24.11	−23.93	−24.49	−5.96	135†
J1022 + 1001	60.78	-1.60×10^{-16}	−24.15	−22.88	−23.11	−24.15	−4.87	161	−23.99	−23.80	−24.24	−24.31	−5.03	113	−24.16	−23.80	−24.26	−24.37	−5.09	98
J1024−0719	193.72	-6.95×10^{-16}	−23.79	−23.46	−23.46	−23.97	−5.63	243	−23.92	−23.95	−23.94	−24.19	−5.85	147	−24.05	−23.99	−23.95	−24.33	−5.98	109
J1045−4509	133.79	-3.16×10^{-16}	−23.92	−23.61	−23.46	−23.96	−4.32	3243†	−24.13	−24.02	−23.94	−24.24	−4.61	1684†	−24.23	−24.01	−23.99	−24.22	−4.59	1755†
J1300 + 1240	160.81	-2.95×10^{-15}	−23.97	−23.52	−23.44	−24.00	−5.15	734†	−23.84	−23.79	−24.13	−24.08	−5.23	611†	−23.95	−23.79	−24.10	−24.10	−5.25	577†
J1435−6100	106.98	-2.80×10^{-16}	−24.29	−23.64	−23.54	−24.31	−4.48	1217	−24.20	−24.04	−24.17	−24.48	−4.66	819	−24.40	−24.18	−24.22	−24.57	−4.74	668
J1455−3330	125.20	-3.81×10^{-16}	−24.12	−23.37	−23.25	−24.14	−5.09	475†	−24.29	−24.13	−23.89	−24.38	−5.33	275†	−24.38	−24.07	−23.88	−24.41	−5.37	253†
J1518 + 0205A	180.06	-1.34×10^{-15}	−23.68	−22.61	−22.86	−23.73	−3.97	6640	−23.53	−23.74	−23.79	−23.85	−4.09	5045	−23.85	−23.74	−23.79	−23.96	−4.20	3897
J1537 + 1155	26.38	-1.69×10^{-15}	−22.87	−22.09	−22.25	−22.85	−2.36	1998†	−23.39	−22.95	−23.38	−23.68	−3.19	297†	−23.40	−22.95	−23.39	−23.70	−3.21	282†
J1603−7202	67.38	-7.10×10^{-17}	−24.33	−23.60	−23.52	−24.35	−4.42	1040†	−24.39	−23.90	−24.07	−24.43	−4.49	876†	−24.50	−23.95	−24.07	−24.58	−4.65	613†
J1623−2631	90.29	-5.47×10^{-15}	−23.95	−23.45	−23.52	−24.00	−4.20	364†	−24.16	−23.76	−24.16	−24.16	−4.36	250†	−24.24	−23.79	−24.15	−24.49	−4.69	117†
J1629−6902	166.65	-2.78×10^{-16}	−24.13	−23.70	−23.29	−24.23	−5.17	771	−24.14	−24.12	−24.11	−24.37	−5.31	559	−24.36	−24.18	−24.11	−24.49	−5.43	423
J1640 + 2224	316.12	-2.83×10^{-16}	−23.58	−23.52	−22.98	−23.56	−5.11	5659†	−23.79	−23.85	−23.73	−24.02	−5.57	1954†	−23.84	−23.86	−23.73	−24.05	−5.60	1819†
J1643−1224	216.37	-8.66×10^{-16}	−23.69	−23.36	−23.19	−23.80	−4.41	5447†	−23.95	−23.80	−23.86	−23.97	−4.58	3658†	−23.97	−23.78	−23.96	−23.97	−4.58	3627†
J1701−3006A	190.78	$+4.80 \times 10^{-15}$	−24.10	−23.37	−23.42	−24.01	−4.36	*	−24.11	−23.88	−23.97	−24.23	−4.58	*	−24.27	−23.85	−24.00	−24.41	−4.76	*
J1701−3006B	278.25	$+2.71 \times 10^{-14}$	−23.96	−23.48	−23.07	−23.94	−4.62	*	−24.06	−23.89	−23.54	−24.05	−4.73	*	−24.16	−23.92	−23.56	−24.16	−4.84	*
J1701−3006C	262.71	$+2.20 \times 10^{-15}$	−23.91	−23.45	−23.18	−23.84	−4.47	*	−23.94	−23.94	−23.78	−24.11	−4.74	*	−24.13	−23.93	−23.76	−24.20	−4.82	*
J1713 + 0747	218.81	-4.08×10^{-16}	−23.65	−23.16	−23.13	−23.64	−4.90	2401†	−23.98	−24.02	−23.81	−24.08	−5.34	865†	−24.01	−23.94	−23.78	−24.15	−5.40	748†
J1744−1134	245.43	-5.39×10^{-16}	−23.88	−23.47	−23.39	−23.93	−5.78	386†	−23.67	−23.91	−23.95	−23.98	−5.83	345†	−23.83	−23.87	−23.97	−24.05	−5.90	296†

TABLE III. (*Continued*)

PULSAR	ν (Hz)	$\dot{\nu}$ (Hz s^{-1})	S3 $\log h_0^{95\%}$ H1	S3 $\log h_0^{95\%}$ H2	S3 $\log h_0^{95\%}$ L1	S3 $\log h_0^{95\%}$ Joint	S3 $\log\varepsilon$	S3 Ratio	S4 $\log h_0^{95\%}$ H1	S4 $\log h_0^{95\%}$ H2	S4 $\log h_0^{95\%}$ L1	S4 $\log h_0^{95\%}$ Joint	S4 $\log\varepsilon$	S4 Ratio	S3 and S4 $\log h_0^{95\%}$ H1	S3 and S4 $\log h_0^{95\%}$ H2	S3 and S4 $\log h_0^{95\%}$ L1	S3 and S4 $\log h_0^{95\%}$ Joint	S3 and S4 $\log\varepsilon$	S3 and S4 Ratio
J1745−0952	51.61	-2.53×10^{-16}	−23.99	−23.42	−23.40	−24.00	−3.68	1328	−24.33	−23.83	−24.15	−24.38	−4.06	552	−24.28	−23.83	−24.16	−24.38	−4.06	551
J1748−2446A	172.96	$+2.54\times10^{-16}$	−24.19	−23.66	−23.61	−24.19	−3.75	*	...	...	...	...	...	...	...	...	...	...	...	...
J1748−2446C	118.54	$+8.52\times10^{-15}$	−24.18	−23.12	−23.58	−24.18	−4.01	*	−24.27	−23.95	−24.23	−24.50	−4.34	*	−24.41	−23.96	−24.24	−24.54	−4.37	*
J1756−2251	35.14	-1.26×10^{-15}	−23.71	−22.84	−23.04	−23.70	−2.95	1209	−23.83	−23.25	−23.59	−23.78	−3.04	999	−23.84	−23.26	−23.59	−23.80	−3.05	971
J1757−5322	112.74	-3.34×10^{-16}	−24.16	−23.50	−23.45	−24.21	−4.81	605	−24.16	−24.14	−24.16	−24.44	−5.04	353	−24.24	−24.13	−24.13	−24.43	−5.03	360
J1801−1417	275.85	-4.02×10^{-16}	−23.70	−23.40	−23.15	−23.82	−5.07	2783	−23.92	−23.82	−23.89	−24.14	−5.39	1347	−23.99	−23.87	−23.86	−24.20	−5.46	1156
J1802−2124	79.07	-4.50×10^{-16}	−24.05	−23.43	−23.53	−24.01	−3.91	1688	−24.11	−24.13	−24.14	−24.34	−4.24	791	−24.17	−24.09	−24.15	−24.23	−4.13	1022
J1804−0735	43.29	-8.75×10^{-16}	−23.86	−23.24	−23.13	−23.83	−2.81	3409	−24.10	−23.70	−24.07	−24.26	−3.24	1266	−24.24	−23.72	−24.07	−24.31	−3.28	1146
J1804−2717	107.03	-4.68×10^{-16}	−24.08	−23.47	−23.53	−24.02	−4.64	663	−24.15	−24.15	−24.23	−24.36	−4.97	305	−24.28	−24.16	−24.22	−24.32	−4.94	329
J1807−2459A	326.86	$+4.87\times10^{-16}$	−23.73	−23.30	−23.02	−23.79	−5.01	*	−23.98	−23.79	−23.85	−24.12	−5.35	*	−24.07	−23.84	−23.86	−24.20	−5.42	*
J1810−2005	30.47	-1.40×10^{-16}	−23.22	−22.24	−22.70	−23.24	−2.23	13340	−23.40	−23.13	−23.36	−23.68	−2.66	4920	−23.57	−23.13	−23.37	−23.69	−2.68	4768
J1823−3021A	367.65	-1.14×10^{-13}	−23.74	−23.46	−23.36	−23.77	−4.02	671	...	...	...	...	...	...	...	...	...	...	...	...
J1824−2452	327.41	-1.74×10^{-13}	−23.93	−23.41	−23.05	−23.92	−4.88	321†	−23.87	−23.77	−23.68	−24.09	−5.06	214†	−24.03	−23.87	−23.70	−24.19	−5.16	171†
J1843−1113	541.81	-2.82×10^{-15}	−23.24	−23.14	−22.77	−23.30	−5.09	5429	−23.59	−23.57	−23.43	−23.85	−5.65	1508	−23.61	−23.61	−23.42	−23.89	−5.69	1370
J1857+0943	186.49	-6.20×10^{-16}	−23.72	−23.50	−23.41	−23.71	−4.92	1223†	−23.97	−23.80	−24.04	−24.31	−5.52	309†	−24.00	−23.82	−24.07	−24.30	−5.51	313†
J1905+0400	264.24	-3.39×10^{-16}	−23.89	−23.22	−23.27	−23.83	−5.17	2185	−23.88	−23.72	−23.81	−23.88	−5.22	1937	−24.05	−23.84	−23.84	−24.02	−5.36	1410
J1909−3744	339.32	-1.61×10^{-15}	−23.82	−23.41	−22.97	−23.92	−5.55	1725†	−23.84	−23.89	−23.67	−24.00	−5.63	1437†	−23.88	−23.97	−23.72	−24.13	−5.76	1060†
J1910−5959A	306.17	-2.88×10^{-16}	−23.93	−23.35	−23.10	−24.01	−5.01	4950	−23.79	−23.59	−23.76	−24.07	−5.07	4330	−24.01	−23.80	−23.78	−24.21	−5.20	3178
J1910−5959B	119.65	$+1.14\times10^{-14}$	−24.28	−23.04	−23.36	−24.29	−4.47	*	−23.61	−24.02	−24.06	−24.20	−4.38	*	−24.30	−24.02	−24.07	−24.39	−4.57	*
J1910−5959C	189.49	-7.90×10^{-17}	−24.03	−23.60	−23.37	−24.04	−4.62	7018	−24.18	−24.07	−23.97	−24.23	−4.81	4470	−24.32	−24.10	−24.00	−24.39	−4.97	3107
J1910−5959D	110.68	-1.18×10^{-14}	−24.20	−23.35	−23.26	−24.12	−4.23	369	−24.40	−24.05	−24.17	−24.48	−4.60	158	−24.41	−24.07	−24.12	−24.42	−4.53	182
J1910−5959E	218.73	$+2.09\times10^{-14}$	−23.98	−23.71	−23.30	−24.05	−4.75	*	−24.09	−23.96	−23.99	−24.35	−5.05	*	−24.15	−24.01	−23.99	−24.34	−5.04	*
J1911+0101A	276.36	$+5.03\times10^{-16}$	−23.56	−23.38	−23.05	−23.79	−4.43	*	−23.89	−23.83	−23.83	−24.12	−4.76	*	−24.07	−23.84	−23.81	−24.22	−4.86	*
J1911+0101B	185.72	$+6.90\times10^{-17}$	−23.70	−23.43	−23.30	−23.78	−4.07	*	−24.05	−24.01	−24.05	−24.24	−4.53	*	−23.96	−24.08	−23.99	−24.13	−4.43	*
J1911−1114	275.81	-1.08×10^{-15}	−23.85	−23.51	−23.00	−23.84	−5.14	2188†	−23.99	−23.80	−23.71	−24.07	−5.37	1288†	−24.04	−23.86	−23.70	−24.12	−5.43	1139†
J1939+2134	641.93	-4.33×10^{-14}	−23.17	−23.22	−22.51	−23.37	−5.05	2323†	−23.41	−23.44	−23.33	−23.68	−5.36	1146†	−23.46	−23.49	−23.31	−23.78	−5.47	899†
J1955+2908	163.05	-7.91×10^{-16}	−23.82	−23.61	−23.35	−23.88	−4.20	4088†	−24.22	−23.94	−24.02	−24.32	−4.64	1487†	−24.26	−23.96	−23.99	−24.40	−4.72	1223†
J1959+2048	622.12	-6.52×10^{-15}	−23.30	−23.04	−22.65	−23.35	−5.38	3220†	−23.66	−23.37	−23.54	−23.79	−5.82	1163†	−23.68	−23.36	−23.54	−23.82	−5.85	1080†
J2019+2425	254.16	-4.54×10^{-16}	−23.79	−23.49	−23.23	−23.93	−5.41	1628†	−23.93	−23.89	−23.79	−24.16	−5.64	970†	−23.93	−23.91	−23.75	−24.17	−5.65	950†
J2051−0827	221.80	-6.27×10^{-16}	−23.97	−23.49	−23.16	−24.05	−5.26	852†	−23.83	−23.79	−23.77	−24.02	−5.23	917†	−24.00	−23.83	−23.77	−24.11	−5.32	740†
J2124−3358	202.79	-8.45×10^{-16}	−24.08	−23.56	−23.35	−24.06	−5.90	165†	−23.91	−23.91	−24.00	−24.13	−5.98	139†	−24.20	−24.03	−23.99	−24.31	−6.15	93†
J2129−5721	268.36	-1.49×10^{-15}	−23.82	−23.45	−23.22	−23.89	−4.96	1809†	−24.02	−23.95	−23.90	−24.19	−5.27	892†	−24.01	−23.91	−23.89	−24.18	−5.25	926†
J2140−2310A	90.75	$+4.27\times10^{-16}$	−24.25	−23.48	−23.52	−24.23	−3.82	*	−24.31	−24.00	−24.06	−24.45	−4.04	*	−24.45	−23.99	−24.10	−24.55	−4.14	*
J2145−0750	62.30	-1.15×10^{-16}	−24.14	−23.18	−23.53	−24.18	−4.69	326†	−24.23	−23.76	−24.24	−24.45	−4.97	173†	−24.31	−23.78	−24.26	−24.47	−4.98	167†
J2229+2643	335.82	-1.65×10^{-16}	−23.58	−23.31	−23.08	−23.64	−5.17	5747	−23.77	−23.51	−23.72	−23.89	−5.41	3253	−23.89	−23.56	−23.71	−24.13	−5.65	1885
J2317+1439	290.25	-2.04×10^{-16}	−23.41	−23.40	−23.17	−23.55	−4.82	9996†	−23.89	−23.91	−23.79	−24.17	−5.44	2406†	−23.86	−23.90	−23.80	−24.15	−5.43	2500†
J2322+2057	207.97	-4.20×10^{-16}	−23.86	−23.48	−23.17	−24.07	−5.44	900†	−24.01	−23.91	−23.85	−24.19	−5.56	673†	−24.07	−23.96	−23.96	−24.26	−5.63	578†

TABLE IV. Upper limits including GEO 600 for the two fastest pulsars in the analysis.

			S3				S4				S3 and S4			
			$\log h_0^{95\%}$		$\log\varepsilon$	Ratio	$\log h_0^{95\%}$		$\log\varepsilon$	Ratio	$\log h_0^{95\%}$		$\log\varepsilon$	Ratio
PULSAR	ν (Hz)	$\dot{\nu}$ (Hz s^{-1})	GEO	Joint			GEO	Joint			GEO	Joint		
J1843−1113	541.81	-2.82×10^{-15}	*	−23.32	−5.12	5167	−22.45	−23.85	−5.65	1508	−22.45	−23.90	−5.67	1348
J1939+2134	641.93	-4.33×10^{-14}	−22.23	−23.37	−5.05	2323†	−22.68	−23.66	−5.34	1189†	−22.71	−23.77	−5.46	914†

into account the better sensitivity during the S4 run. For all except PULSAR9 the h_0 values were reduced by ∼half, with PULSAR9 being so strong that its amplitude was reduced by a factor of ∼20. These signals were injected for the second half of the run from 8 March 2005 onwards. The updated h_0 values are shown in Table I. There were also an additional two signals (PULSAR10 and 11), simulated to be from pulsars in binary systems, injected for the last day of the run. The binary pulsar injections allowed the testing of the binary timing code described in Sec. III B as the injection code and extraction code were written independently. The binary injection signal parameters for PULSAR10 and PULSAR11 were taken from PULSAR3 and 8, respectively, with the frequencies changed, and amplitudes increased to make sure they were visible over the short injection time. The frequency, amplitude, and binary system parameters are shown in Table II. The binary system parameters were chosen to have one in a relatively eccentric orbit and one in a circular orbit. We chose fairly short periods, so that they would have completed or nearly completed at least one full orbit during the injection. The T_0 values are given in the pulsar rest frame.

For the recovery of the binary system injections, the BT model was used, although, as no relativistic parameters were included, any of the models could have been used.

The extracted amplitude and phase pdfs, after corrections described below, are shown in Fig. 8. The observed phase consistency between the detectors means that joint likelihoods, using all three detectors, can be calculated. In general, the values of h_0 are well matched with the injection values. It can again be seen that for the strongest signals the narrow pdfs are offset from the injected value in h_0, reflecting the calibration uncertainties of 5%–10%.

The binary pulsar injections show matches to their injected values. This is a good confirmation that the binary timing code can track the phase well and has no significant errors.

3. Calibration issues

A brief note should be made of the effect of calibrations on the above extracted pulsar hardware injections. The injections were, for the most part, analyzed using exactly the same pipeline as applied to the general known pulsar analysis. However, due to the nature of the hardware injections some additional post-processing of the results has had to be applied. To calculate the amplitude and phase of the injections, when applying forces to the interferometer end test masses, a reference calibration must be used. These reference calibrations are different for each interferometer. For both S3 and S4 these reference calibrations differed by small, but not insignificant amounts, from the final calibration used when extracting the signals, meaning that upon extracting the signals the amplitude and phase appear offset from the injected values. As the differences between the reference and final calibrations are different for each interferometer, there will also be slight offsets between the extracted parameters between detectors. The extracted signals from each interferometer therefore have had to be adjusted to reflect these differences, determined independently of the hardware injections, and correct them so as to give the same input signal. This allows the combined joint upper limits to be produced.

[1] R. J. Dupuis and G. Woan, Phys. Rev. D **72**, 102002 (2005).
[2] B. Abbott *et al.* (LIGO Scientific Collaboration), Phys. Rev. D **69**, 082004 (2004).
[3] B. Abbott *et al.* (LIGO Scientific Collaboration), Phys. Rev. Lett. **94**, 181103 (2005).
[4] B. Abbott *et al.* (LIGO Scientific Collaboration), arXiv:gr-qc/0605028.
[5] P. Jaranowski, A. Królak, and B. F. Schutz, Phys. Rev. D **58**, 063001 (1998).
[6] M. Zimmermann and E. Szedenits, Jr., Phys. Rev. D **20**, 351 (1979).
[7] D. I. Jones and N. Andersson, Mon. Not. R. Astron. Soc. **331**, 203 (2002).
[8] S. Bonazzola and E. Gourgoulhon, Astron. Astrophys. **312**, 675 (1996).
[9] H. Hirakawa, K. Tsubono, and M. K. Fujimoto, Phys. Rev. D **17**, 1919 (1978).
[10] T. Suzuki, First Edoardo Amaldi Conference on Gravitational Wave Experiments (1995) p. 115.
[11] J. Hough *et al.*, Nature (London) **303**, 216 (1983).
[12] M. Hereld, Ph.D. thesis, California Institute of Technology, 1983.
[13] Australia Telescope National Facility Pulsar Catalogue,

http://www.atnf.csiro.au/research/pulsar/psrcat/.
[14] R. J. Dupuis, Ph.D. thesis, University of Glasgow, 2004.
[15] http://einstein.phys.uwm.edu/FinalS3Results/
[16] B. Abbott *et al.* (LIGO Scientific Collaboration), Phys. Rev. D **72**, 102004 (2005).
[17] B. Abbott *et al.* (LIGO Scientific Collaboration), All-Sky LIGO Search for Periodic Gravitational Waves in the S4 Data (unpublished).
[18] F. Acernese *et al.*, Classical Quantum Gravity **22**, S869 (2005).
[19] T. Creighton, Classical Quantum Gravity **20**, S853 (2003).
[20] J. H. Taylor and J. M. Weisberg, Astrophys. J. **345**, 434 (1989).
[21] J. R. Smith *et al.*, Classical Quantum Gravity **21**, S1737 (2004).
[22] S. Hild *et al.*, J. Phys.: Conf. Ser. **32**, 66 (2006).
[23] http://www.atnf.csiro.au/research/pulsar/tempo.
[24] M. D. Pitkin and G. Woan, arXiv:gr-qc/0703152 [Phys. Rev. D (to be published)].
[25] C. Lange *et al.*, Mon. Not. R. Astron. Soc. **326**, 274 (2001).
[26] R. N. Manchester *et al.*, Astron. J. **129**, 1993 (2005).
[27] Jodrell Bank Crab Pulsar Monthly Ephemeris, http://www.jb.man.ac.uk/research/pulsar/crab.html.
[28] G. Hobbs *et al.*, Mon. Not. R. Astron. Soc. **353**, 1311 (2004).
[29] F. E. Marshall *et al.*, Astrophys. J. **603**, 682 (2004).
[30] S. M. Ransom *et al.*, Science **307**, 892 (2005).
[31] J. M. Cordes and D. J. Helfand, Astrophys. J. **239**, 640 (1980).
[32] Z. Arzoumanian *et al.*, Astrophys. J. **422**, 671 (1994).
[33] G. Hobbs, A. G. Lyne, and M. Kramer (unpublished).
[34] G. Hobbs *et al.*, Mon. Not. R. Astron. Soc. **360**, 974 (2005).
[35] J. M. Cordes and G. Greenstein, Astrophys. J. **245**, 1060 (1981).
[36] D. I. Jones, Phys. Rev. D **70**, 042002 (2004).
[37] M. Pitkin and G. Woan, Classical Quantum Gravity **21**, S843 (2004).
[38] http://www.lsc-group.phys.uwm.edu/daswg/projects/lalapps.html.
[39] D. A. Frail and J. M. Weisberg, Astron. J. **100**, 743 (1990).
[40] A. Lyne and F. Graham-Smith, *Pulsar Astronomy* (Cambridge University Press, Cambridge, England, 1998).
[41] I. S. Shklovskii, Sov. Astron. **13**, 562 (1970).
[42] E. S. Phinney, ASP Conf. Ser. 50: Structure and Dynamics of Globular Clusters (1993).
[43] S. E. Thorsett and D. Chakrabarty, Astrophys. J. **512**, 288 (1999).
[44] M. Bejger, T. Bulik, and P. Haensel, Mon. Not. R. Astron. Soc. **364**, 635 (2005).
[45] D. J. Nice *et al.*, Astrophys. J. **634**, 1242 (2005).
[46] B. D. Lackey, Undergraduate honors thesis, The Pennsylvania State University, 2006.
[47] B. D. Lackey, M. Nayyar, and B. J. Owen, Phys. Rev. D **73**, 024021 (2006).
[48] M. Bejger and P. Haensel, Astron. Astrophys. **396**, 917 (2002).
[49] M. Bejger and P. Haensel, Astron. Astrophys. **405**, 747 (2003).
[50] I. A. Morrison *et al.*, Astrophys. J. **617**, L135 (2004).
[51] J. M. Lattimer and B. F. Schutz, Astrophys. J. **629**, 979 (2005).
[52] M. Kramer *et al.*, Science **314**, 97 (2006).
[53] M. Pitkin *et al.* (LIGO Scientific Collaboration), Classical Quantum Gravity **22**, S1277 (2005).
[54] M. Zimmerman, Nature (London) **271**, 524 (1978).
[55] C. Palomba, Astron. Astrophys. **354**, 163 (2000).
[56] B. Owen, Phys. Rev. Lett. **95**, 211101 (2005).
[57] U. Weiland *et al.*, Classical Quantum Gravity **21**, S861 (2004).